

# Chemical Bonding in Homogenous Catalysis – Seen Through the Eyes of Vibrational Spectroscopy

Elfi Kraka and Marek Freindorf, Department of Chemistry, Southern Methodist University, Dallas, TX, United States

© 2022 Elsevier Inc. All rights reserved.

<b>1</b>	<b>Introduction</b>	<b>1</b>
<b>2</b>	<b>Methodology</b>	<b>3</b>
2.1	Monitoring Chemical Reactions	3
2.1.1	Currently used strategies	3
2.1.2	The Unified Reaction Valley Approach (URVA)	3
2.2	Characterizing Chemical Bonds	5
2.2.1	Some popular approaches	5
2.2.2	The local vibrational mode analysis (LMA)	5
<b>3</b>	<b>Applications</b>	<b>7</b>
3.1	Au-Catalyzed[3,3]-Sigmatropic Rearrangement of Allyl Acetate	7
3.2	Re-Catalyzed CO <sub>2</sub> Cycloaddition to Epoxides	10
3.3	$\alpha$ -ketoamide Inhibitor for SARS-CoV-2 Main Protease	12
3.3.1	Gas phase reaction	16
3.3.2	Protein reaction	17
<b>4</b>	<b>Computational Details</b>	<b>19</b>
<b>5</b>	<b>Conclusions</b>	<b>20</b>
<b>6</b>	<b>Acknowledgments</b>	<b>21</b>
<b>Appendix A</b>	<b>Supplementary Material</b>	<b>21</b>
<b>References</b>		<b>22</b>

## Abstract

We introduce two new tools for the analysis of bond forming/breaking processes taking place during catalytic reactions, the Unified Reaction Valley Approach (URVA) and the Local Mode Analysis (LMA), both being based on vibrational spectroscopy. We discuss how URVA and LMA complement currently used computational approaches and provide valuable insights into catalytic processes, supporting current design efforts aiming at more efficient and environmentally friendly catalysts. Three examples are presented; Au-catalyzed [3,3]-sigmatropic rearrangement of allyl acetate, Re-catalyzed CO<sub>2</sub> cycloaddition to epoxides, and  $\alpha$ -ketoamide inhibitors for SARS-CoV-2 main protease. We hope that URVA and LMA will become routinely applied tools in computational catalysis and also enter the classroom.

## Key Points

- Basic principles of catalysis
- Bond breaking/forming processes in catalysis
- Currently applied computational approaches to catalysis
- URVA - a new tool for the decrypting of mechanistic details
- LMA - a new tool providing a quantitative measure of bond strength
- Examples: Au-catalyzed[3,3]-sigmatropic rearrangement of allyl acetate; Re-catalyzed CO<sub>2</sub> cycloaddition to epoxides;  $\alpha$ -ketoamide inhibitors for SARS-CoV-2 main protease

## 1 Introduction

Catalysis is a central topic in chemistry and plays a pivotal role in tackling the grand challenges of the 21st Century. There is an increasing demand in goods and fine chemicals caused by the predicted rise in global population or climate change requesting refined much more environmentally friendly production procedures. More than 90% of all commercial chemical compounds are synthesized with the help of a catalyst at one stage of their production.<sup>1–5</sup> Grand View Research, Inc. reports that the global catalyst market size is expected to reach USD 34.1 billion by 2025.<sup>6</sup>

As prognosticated in their combined Technology Roadmap Report of the International Energy Agency, the International Council of Chemical Associations and the Gesellschaft für Chemische Technik und Biotechnologie, more efficient use of catalysts and related processes could reduce the energy consumption in industrial processes by 20%–40% and greenhouse gas emission (GHG) by 30%–40% by 2050.<sup>7</sup> In particular, enzyme engineering and biocatalysis is a growing field, which is inspired by enzymatic processes developed by Nature.<sup>8–14</sup> Biocatalysts have become an essential tool in industrial biotechnology being aimed at producing sustainably cheaper chemical products in chemical and pharmaceutical industries in an eco-friendly way.<sup>15</sup> These facts clearly show the urgent need to continuously optimize existing catalysts and to design new ones, a challenging enterprise for both experimental and computational chemists. It is not surprising that so far 21 Chemistry Nobel Prizes (the most recent in 2021 awarded to Benjamin List and David MacMillan for the development of asymmetric organocatalysis) have been associated with discoveries related to catalysts or catalysis.<sup>16</sup>

As sketched in Fig. 1 homogenous catalysts generally lower the barrier of a chemical reaction leading to higher rate constants, predominantly by facilitating energy consuming bond breaking/forming processes; a well-accepted fact in the chemical community.<sup>1,17,18</sup> A lot of effort has been put into the modeling of catalysis and their catalytic activities, ranging from the design and optimization of catalysts based on quantum chemical calculations,<sup>19–26</sup> automated *in silico* catalyst design,<sup>27</sup> machine learning based procedures<sup>28,29</sup> to quantum computing enhanced computational catalysis,<sup>30</sup> forming the gateway to the next generation of efficient and more environmentally friendly catalysts. However, there is room for further improvement, in particular with regard to (1) monitoring and analyzing the progress of a catalytic reaction at the atomic level, and (2) characterizing the chemical bonds being formed/broken during a catalytic cycle, which are at the focus of this article. Currently used quantum chemical tools are summarized and two new tools are introduced, the Unified Reaction Valley Approach (URVA)<sup>31</sup> and the Local Vibrational Mode Analysis (LMA),<sup>32</sup> both having their roots in vibrational spectroscopy.

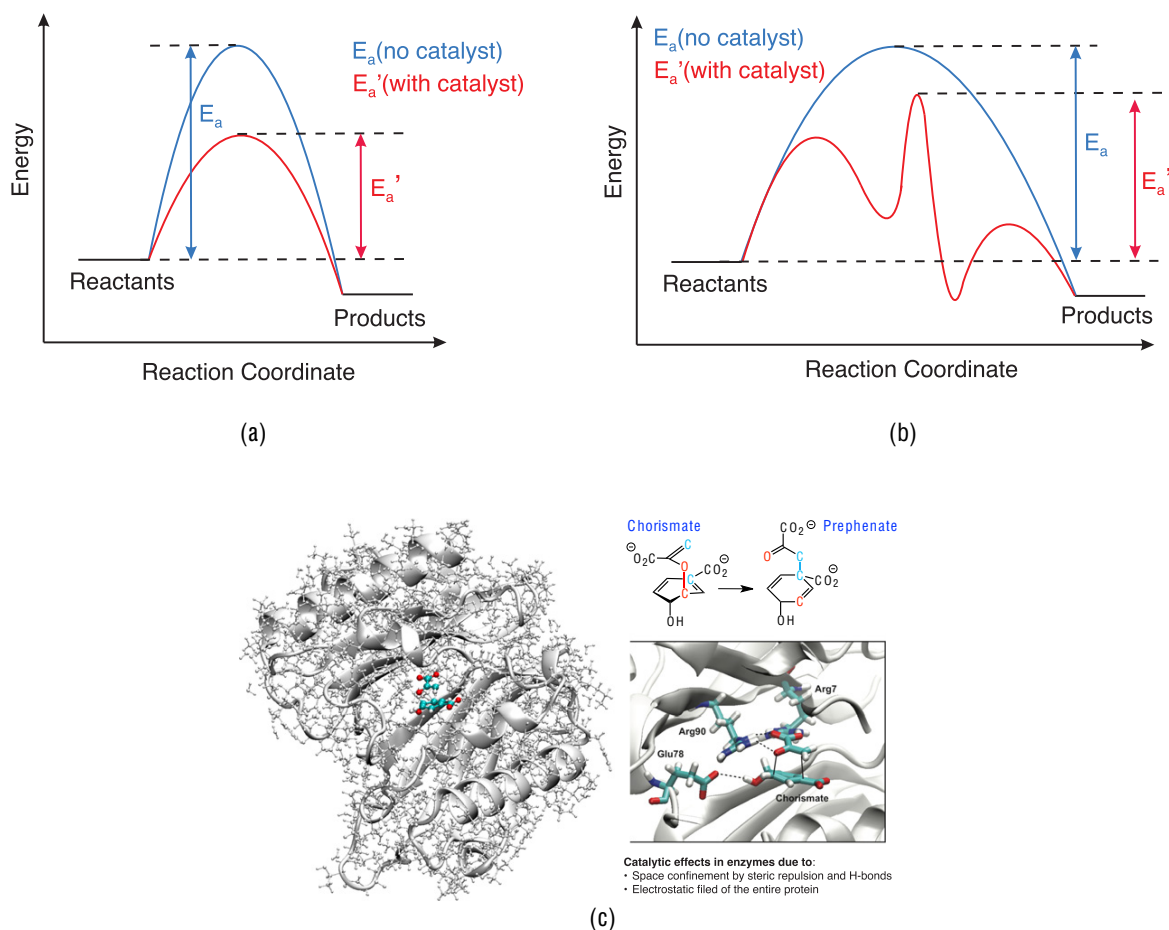


**Fig. 1** Homogenous catalysis: (a) Scenario I: The catalyst reduces the energy barrier. (b) Scenario II: The catalyst splits up the reaction into multiple reaction steps. Each reaction step has a lower energy barrier than the original barrier. (c) Scenario III: Enzyme catalysis, the reaction takes place in the active site pocket of the enzyme, shown for the *Bacillus subtilis* chorismate mutase catalyzed Claisen rearrangement of chorismate. Reproduced from Freindorf, M., Tao, Y., Sethio, D., Cremer, D., Kraka, E., 2018. New mechanistic insights into the claisen rearrangement of chorismate – A unified reaction valley approach study. Mol. Phys. 117, 1172–1192.

## 2 Methodology

### 2.1 Monitoring Chemical Reactions

In this section popular computational strategies for exploring the mechanism of a chemical reaction are summarized followed by short description of URVA.

#### 2.1.1 Currently used strategies

The most elaborate way to model the mechanism of a chemical reaction is to map and analyze the potential energy surface (PES) spanned by the reaction complex (RC, the union of reacting molecules). However, this is a daunting task, considering that the dimensionality of the PES is  $(3N-L) = N_{vib}$  with  $N$ : number of atoms of the RC;  $L$ : number of overall translations and rotations of the RC. Over the past years, different procedure have been developed to construct the PES, even for larger systems aiming toward chemical accuracy.<sup>34–37</sup> Recently machine learning and artificial intelligence have been added to the repertoire.<sup>36,38–40</sup> However, not all locations on the PES are of importance for a chemical reaction, in particular the high energy regions. Therefore, procedures have been developed to focus on reaction paths (RP)s on PES traced by the RC on its way from an entrance to exit channel<sup>41–46</sup> including algorithms for automatically finding RPs<sup>46–50</sup> and methods for working in a reduced dimensional space.<sup>51</sup> Other efforts have been devoted to the analysis of the rich data collected along the RPs. Some representative examples include (1) Monitoring changes of the topological features of the electron density<sup>52,53</sup> or the electron localization function<sup>54</sup> along the RP;<sup>55–57</sup> (2) The reaction force and force constant method, which is aimed at extracting information from higher derivatives of the energy profile taken along the RP,<sup>58–60</sup> where one has to take into account that the energy is a cumulative property and as such the mechanistic information obtained is more of a holistic nature; (3) The discussion of local reactivity descriptors, e.g., the Fukui function, and how they infer reactivity trends along the RP,<sup>61,62</sup> and (4) The recently suggested exploration of the PES with immersive virtual reality.<sup>63</sup> A complementary approach of monitoring the reaction mechanism is pursued in molecular dynamics (MD) simulations as to provide an atomic visualization into the detail of molecular reactions on a femtosecond time scale.<sup>64–67</sup> MD simulations can be performed on a previously constructed PES or alternatively with a direct methodology calculating the trajectories on the fly.<sup>68–70</sup> In contrast to classical MD which relies on Newton's equation, *ab initio* MD is based on the Schrödinger equation. It offers a more realistic simulation of complex molecular systems and processes from first principles.<sup>71,72</sup> Recently MD has also been connected with machine learning procedures.<sup>39,73,74</sup> Finally, on the low end scale, there is the *poor man's approach*, i.e., the mechanism is explored by just focusing on the properties of the stationary points, minima of reactants and products and transition state (TS), where often their proper identification and verification demands the calculation of the reaction path connection of these points.

#### 2.1.2 The Unified Reaction Valley Approach (URVA)

The Unified Reaction Valley Approach (URVA)<sup>75–79</sup> provides the perfect compromise between exploiting the complex PES and tracing the RP on the PES which connects the stationary points. URVA is based on vibrational spectroscopy and the early work of Hofacker,<sup>80</sup> Marcus,<sup>81–83</sup> and Hougen<sup>84</sup> which describes the RC via a vibration of large amplitude along the RP and  $(N_{vib}-1)$  vibrations perpendicular to it, which together define the so-called  $N_{vib}$  dimensional *reaction valley*. This ansatz led to the famous Miller, Handy, and Adams (MHA) reaction path Hamiltonian (RPH)<sup>85</sup> and related work of Kato and Morokuma.<sup>86</sup> A comprehensive review of the URVA methodology can be found in Ref. 31, the theoretical basis and background of URVA has also been thoroughly described in Refs. 76, 87 and 88. In the following, only some essentials are summarized. The central focus of the RPH is on (1) the RP, a curved line in  $N_{vib}$ -dimensional space and (2) the coupling between the large amplitude and the perpendicular vibrations.

During the course of a chemical reaction the RC changes its electronic structure and this is directly registered by the vibrational modes, which are sensitive to even the smallest electronic structure changes. The large amplitude motion along the RP and the vibrations perpendicular to the path change, leading to changes in their coupling. MHA showed in their seminal paper that the magnitude of the reaction path curvature  $\kappa(s) = \|\kappa(s)\|$  at each path point  $s$  can be calculated as the sum over all coupling elements<sup>85</sup>

$$\kappa(s) = \|\kappa(s)\| = [\kappa(s)\kappa(s)]^{1/2} = \left[ \sum_{\mu=2}^{N_{vib}} B_{\mu s}^2(s) \right]^{1/2} \quad (1)$$

Because of this relationship, the  $B_{\mu s}(s)$  coefficients are called *curvature couplings*. In other words, the curving of the reaction path is directly related to chemical change, i.e., important mechanistic features of a reaction such as bond breaking/forming events are reflected by a strong curving of the RP.

Instead of numerically calculating  $\kappa(s)$  via Eq. (1), we developed a fully analytical procedure. Since the RP is a curved line in  $N_{vib}$  dimensional space its direction and curvature can be derived with the Frenet-Serret formalism.<sup>89</sup> The reaction path direction  $\eta(s)$  at a path point  $s$  is given by the unit vector:

$$\eta(s) = \frac{d\tilde{x}(s)}{ds} = -\frac{\tilde{g}(\tilde{x}(s))}{c(s)} \quad (2)$$

where the derivative of the mass-weighted reaction coordinate  $\tilde{x}(s)$  with regard to  $s$  is the normalized mass-weighted gradient vector  $\tilde{g}(s) \equiv \tilde{g}(\tilde{x}(s)) = \mathbf{M}^{1/2}\mathbf{g}(s)$  and  $\mathbf{M}$  is a diagonal matrix of atomic masses. The curvature vector  $\kappa(s)$  is then given by<sup>75,90</sup>

$$\kappa(s) = \frac{d^2\tilde{x}(s)}{ds^2} = \frac{d\eta(s)}{ds} = \frac{-1}{\|\tilde{g}(s)\|} \left( \tilde{f}^x(s)\eta(s) - [(\eta(s))^\dagger \tilde{f}^x(s)\eta(s)]\eta(s) \right) \quad (3)$$

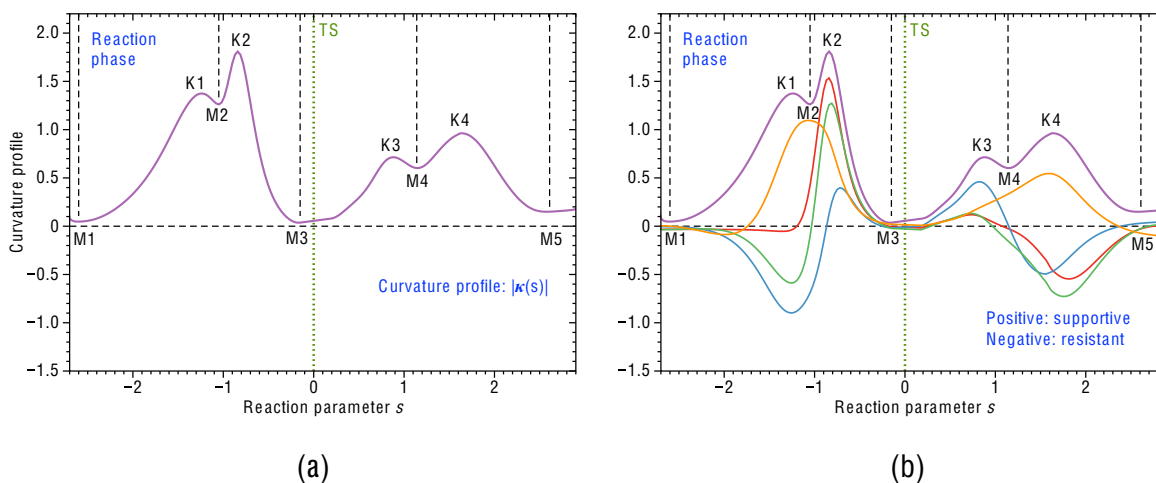


**Fig. 2** (a) Schematic representation of the curvature profile for a model reaction. The scalar curvature  $\kappa(s)$  as a function of the reaction parameter  $s$  is given by the solid purple line. Curvature minima  $M$  and curvature maxima  $K$  are shown. The location of the TS (green symbol) is denoted by a dotted blue line. Start and end of each reaction phase are denoted by dashed black lines. (b) Decomposition of the scalar curvature  $\kappa(s)$  into components. Four different components are shown in orange, red, green and blue color.

Matrix  $\tilde{\mathbf{f}}^x(s)$  is the mass-weighted force constants matrix expressed in Cartesian coordinates. The curvature coupling  $B_{\mu s}(s)$  coefficients can be calculated via

$$B_{\mu s}(s) = \boldsymbol{\eta}(s)^\dagger \frac{d\tilde{\boldsymbol{\ell}}_\mu^g(s)}{ds} = -\tilde{\boldsymbol{\ell}}_\mu^g(s)^\dagger \frac{d\boldsymbol{\eta}_\mu(s)}{ds} = \tilde{\boldsymbol{\ell}}_\mu^g(s)^\dagger \boldsymbol{\kappa}(s) \quad (4)$$

where  $\tilde{\boldsymbol{\ell}}_\mu^g(s)$  corresponds to the generalized mass-weighted normal vibrational mode of vibration  $\mu$  perpendicular to the RP, which can be determined by solving the generalized Wilson equation projecting out at each path point  $s$  in addition to the rotations and translations of the RC also the translational motion along the RP.<sup>90,91</sup>

Monitoring  $\kappa(s)$  along  $s$ , leads to a unique curvature profile for each chemical reaction, with curvature maxima  $K$  and minima  $M$  as schematically shown in Fig. 4(a). The curvature maxima define the locations of electronic structure change, such as charge transfer and charge polarization, rehybridization, bond cleavage, and formation, and also changes in the optimal orientation of the reactants for the reactive collision, whereas the curvature minima correspond to locations with minimal change of the RC, so-called *hidden intermediates*, the transient points separating different chemical events.<sup>78,79,88,92</sup> Different chemical reactions possess different curvature patterns with a different number of reaction phases, which can be used as their fingerprints (Fig. 2).

Further insight into the reaction mechanism, e.g., answering the question of which bond is broken/formed during a certain reaction phase, requires a decomposition of  $\kappa(s)$ . In the original RPH of Miller, Handy, and Adams, a decomposition into  $B_{\mu s}(s)$  coefficients was performed. However, for a mechanistic analysis, the coupling coefficients  $B_{\mu s}(s)$  are of limited use because they refer to normal vibrational modes which tend to delocalize over part or even the entirety of a molecule because of mode-mode coupling, in particular in the case of larger compounds.<sup>91</sup> Therefore, URVA alternatively decomposes  $\kappa(s)$  directly into internal coordinates  $q_n(s)$  used to describe the RC<sup>75</sup> such as bond length, bond angles and dihedral angles or Cremer-Pople puckering coordinates.<sup>93</sup> For each internal coordinate  $q_n$ , a unit column vector  $\mathbf{u}_n$  can be defined<sup>32,87</sup> through its local mass  $m_n^q = G_{n,n}^{-1}$  ( $G_{n,n}$  being a diagonal element of the Wilson G-matrix)<sup>94,95</sup> and the Wilson B-matrix formalism,<sup>91</sup> which connects internal coordinate  $q_n$  to Cartesian coordinates  $\mathbf{x}$  via  $\mathbf{b}_n = dq_n/d\mathbf{x}$ ,

$$\mathbf{u}_n = \frac{\mathbf{M}^{-1/2} \mathbf{b}_n^\dagger}{\|\mathbf{M}^{-1/2} \mathbf{b}_n^\dagger\|} = G_{n,n}^{-1/2} (\mathbf{M}^{-1/2} \mathbf{b}_n^\dagger) \quad (5)$$

with  $G_{n,n} = \mathbf{b}_n \mathbf{M}^{-1} \mathbf{b}_n^\dagger$ .<sup>91</sup>

This leads to a definition of the mass-weighted internal coordinate  $\tilde{q}_n = (m_n^q)^{1/2} q_n$  in terms of  $\boldsymbol{\eta}$  and  $\boldsymbol{\kappa}$ .<sup>87</sup>

$$\frac{d^2 \tilde{q}_n(s)}{ds^2} = \frac{d\boldsymbol{\eta}_n^q(s)}{ds} = \frac{d}{ds} (\mathbf{u}_n^\dagger(s) \boldsymbol{\eta}(s)) = \mathbf{u}_n^\dagger(s) \boldsymbol{\kappa}(s) + \frac{d\mathbf{u}_n^\dagger(s)}{ds} \boldsymbol{\eta}(s) \quad (6)$$

$$= \|\boldsymbol{\kappa}(s)\| \cos \beta_n(s) + \left\| \frac{d\mathbf{u}_n(s)}{ds} \right\| \cos \gamma_n(s) = \kappa_n^q(s) + \eta_n^q(s) \quad (7)$$

The first term on the r.h.s. of Eq. (6) is the projection of  $\mathbf{u}_n(s)$  onto the curvature vector  $\boldsymbol{\kappa}(s)$  leading to the amplitude  $\|\mathbf{u}_n(s)\| \cos \beta_n(s) = \cos \beta_n(s) = \kappa_n^q(s)$  as each  $\mathbf{u}_n$  is a unit vector describing the local motion, which is driven by the internal coordinate  $q_n(s)$ . The amplitude is scaled by the scalar curvature  $\|\boldsymbol{\kappa}(s)\|$  corresponding to the length of the curvature vector in  $N_{vib}$ -dimensional space. The mixed second order term  $\eta_n^q(s)$  is determined by the change in the direction of  $\mathbf{u}_n(s)$  with  $s$  and the tangent vector.

The vector derivative  $du_n(s)/ds$  that is orthogonal to  $u_n(s)$  is projected onto vector  $\eta$  and therefore does not have any information on the curvature.<sup>87</sup> Hence, the curvature contribution of the internal coordinate  $q_n$  is defined by the first term only, i.e.,

$$\kappa_n^q(s) = \mathbf{u}_n^\dagger(s) \boldsymbol{\kappa}(s) \quad (8)$$

In this way, each curvature peak can be associated with a particular chemical event, as sketched in Fig. 2(b). Often, only a few components at a given path point  $s$  contribute to the curving of the RP, which makes the analysis of even larger chemical reactions feasible.<sup>75,92,96–103</sup> It is noteworthy that the sign of a component reflects if it supports (positive sign) or resists (negative sign) the chemical change and that a chemical event, such as bond breaking/forming, can stretch over several phases which we often find in catalysis reactions.<sup>31</sup>

## 2.2 Characterizing Chemical Bonds

In addition to exploring the actual mechanism of the bond breaking/forming processes taking place during the catalytic cycle a comprehensive investigation of the bonding situation at the stationary points leads to further valuable insights. It is frequently speculated that the barrier of a catalytic reaction is lowered by strong bonding interactions in the TS, such as H-bonding, in particular for enzyme reactions.<sup>33</sup> To address these speculations a quantitative measure of bond strength is needed.

### 2.2.1 Some popular approaches

Current popular strategies to assess the strength of a chemical bond or weak chemical interaction include (1) bond dissociation energies (BDE)s<sup>104–106</sup> and related energy decomposition analysis (EDA) schemes<sup>107–109</sup> (2) bond lengths<sup>110,111</sup> and (3) molecular orbital approaches.<sup>112</sup> While these attempts have certainly contributed to our chemical understanding of bonding, one has to realize that EDA schemes are not free from arbitrariness<sup>113</sup> and that molecular orbital approaches depend on the underlying model chemistry.<sup>114</sup> The BDE is a reaction parameter that includes all changes taking place during the dissociation process. Accordingly, it includes any (de)stabilization effects of the fragments to be formed. It reflects the energy needed for bond breaking, but also contains energy contributions due to geometry relaxation and electron density reorganization in the dissociation fragments. Therefore, the BDE is not a suitable measure of the intrinsic strength of a chemical bond and its use may lead to misjudgments, as documented in the literature.<sup>79,115–119</sup> Also the bond length is not always a qualified bond strength descriptor. Numerous cases have been reported illustrating that a shorter bond is not always a stronger bond<sup>95,120–123</sup> Other approaches are based on the inspection of the electrostatic potential,<sup>124</sup> or the topological analysis of the electron density via Bader's quantum theory of atoms in molecules (QTAIM) approach.<sup>125–127</sup> Electrostatic potentials face limitations when used to predict the strength of an interaction or chemical bond because they do not cover the kinetic energy contributions.<sup>117</sup> The topological analysis of the electron density can be useful to uncover possible attractive contacts between two atoms via the existence of a maximum electron density path (i.e., bond path) with a bond critical point connecting the two nuclei under consideration.<sup>128</sup> However, the sole existence of a bond path and a bond critical point does not necessarily imply the existence of a chemical bond; in particular the QTAIM description of weak chemical interactions may be problematic.<sup>129–135</sup> In this situation, vibrational spectroscopy offers a powerful alternative for exploring what are the main contributions to bonding and weak chemical interactions in a compound due to specific atom-atom interactions.

### 2.2.2 The local vibrational mode analysis (LMA)

The idea of characterizing a chemical bond via the stretching force constant dates back to the 1920s and 1930s and includes the well-known *Badger rule*, an inverse power relationship between bond length and stretching force constant.<sup>136</sup> While this rule works fine for diatomic molecules, its extension to polyatomic molecules has turned out to be a major obstacle,<sup>32,137</sup> because normal vibrational modes tend to delocalize over the molecule rather than being localized in a specific bond.<sup>91,138</sup> This disqualifies the related normal mode stretching force constants as a suitable bond strength measure. The local vibrational mode analysis (LMA), originally developed by Konkoli and Cremer,<sup>94,95,121,122,139</sup> has solved this problem which has led to a new measure of the intrinsic strength of a chemical bond or weak chemical interaction and a generalized Badger rule<sup>137</sup> being based on local mode force constants. A comprehensive discussion of the underlying theory of LMA, following two independent routes to derive local vibrational modes, is given in Ref. 32. In the following some essentials are summarized.

There are two coupling mechanisms between vibrational modes, *mass coupling* and *electronic coupling* as reflected in the Euler-Lagrange equation  $L(\mathbf{q}, \dot{\mathbf{q}})$  of the vibrational mode, given here in internal coordinates  $\mathbf{q}$ <sup>140</sup>:

$$L(\mathbf{q}, \dot{\mathbf{q}}) = T(\dot{\mathbf{q}}) - V(\mathbf{q}) \quad (9)$$

$$= \underbrace{\frac{1}{2} \dot{\mathbf{q}}^\dagger \mathbf{G}^{-1} \dot{\mathbf{q}}}_{\text{mass coupling}} - \underbrace{\frac{1}{2} \mathbf{q}^\dagger \mathbf{F}^l \mathbf{q}}_{\text{electronic coupling}} \quad (10)$$

$T(\dot{\mathbf{q}})$  is the kinetic and  $V(\mathbf{q})$  potential energy of the vibrational mode, where the local mode theory uses a harmonic potential.<sup>94,95</sup> The mass coupling in Eq. (10) is related to the off-diagonal elements of the Wilson  $\mathbf{G}$  matrix, reflecting pairwise kinetic coupling between the internal coordinates,<sup>140</sup> and the electronic coupling in Eq. (10) is related to the off-diagonal elements of the force constant matrix  $\mathbf{F}^l$ . Solving Eq. (10), the Wilson equation of vibrational spectroscopy is obtained,<sup>140–142</sup>

$$\mathbf{F}^l \mathbf{D} = \mathbf{G}^{-1} \mathbf{D} \mathbf{A} \quad (11)$$

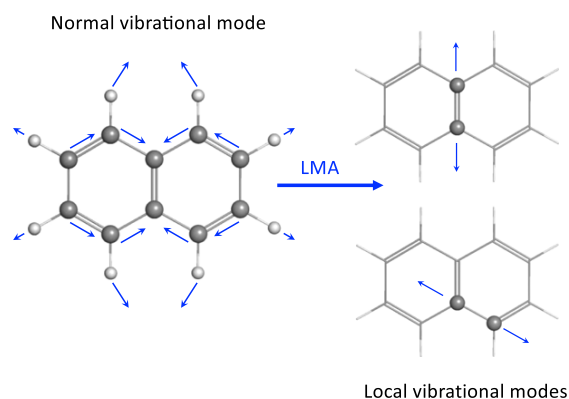


**Fig. 3** Illustration of normal versus local vibrational modes.

Matrix  $\mathbf{D}$  contains the normal mode vectors  $\mathbf{d}_\mu$  in internal coordinates  $\mathbf{q}$  as column vectors with  $\mu = (1, \dots, N_{\text{vib}})$ . The diagonal matrix  $\mathbf{\Lambda}$  collects the normal vibrational eigenvalues  $\lambda_\mu = 4\pi^2 c^2 \omega_\mu$ , where  $\omega_\mu$  represents the harmonic vibrational frequency of normal mode  $\mathbf{d}_\mu$  given in  $\text{cm}^{-1}$ ,  $c$  is the speed of light. The vibrational problem requires the calculation of the analytical second derivatives of the molecular energy, which is generally solved in terms of Cartesian coordinates  $\mathbf{x}$ .

$$\mathbf{f}^{\mathbf{x}} \mathbf{L} = \mathbf{M}^{-1} \mathbf{\Lambda} \mathbf{L} \quad (12)$$

where  $\mathbf{f}^{\mathbf{x}}$  is the force constant matrix in Cartesian coordinates and matrix  $\mathbf{L}$  collects the vibrational eigenvectors  $\mathbf{l}_\mu$  in Cartesian coordinates. In addition, the force constant matrix can be written in terms of normal coordinates  $\mathbf{Q}$  as<sup>143–145</sup>

$$\mathbf{K} = \mathbf{F}^{\mathbf{Q}} = \mathbf{L}^{\dagger} \mathbf{f}^{\mathbf{x}} \mathbf{L} \quad (13)$$

Force constant matrix  $\mathbf{K}$  is diagonal, i.e. the transformation to normal coordinates  $\mathbf{Q}$  via Eq. (13), which is a routine part of a quantum chemical frequency calculation, eliminates the electronic coupling, however it does not eliminate the mass-coupling, which often has been overlooked.

Konkoli and Cremer eliminated the mass-coupling via mass-decoupled Euler-Lagrange equations<sup>94,95</sup>:

$$\begin{aligned} p_n &= \frac{\delta L(\mathbf{q}, \dot{\mathbf{q}})}{\delta \dot{q}_n} \neq 0, \quad \dot{p}_n = \frac{\delta V(\mathbf{q})}{\delta q_n} \neq 0, \\ p_m &= \frac{\delta L(\mathbf{q}, \dot{\mathbf{q}})}{\delta \dot{q}_m} = 0, \quad \dot{p}_m = \frac{\delta V(\mathbf{q})}{\delta q_m} = 0, \quad \forall m \neq n \end{aligned} \quad (14)$$

in which only the masses of the atomic fragment  $\phi_n$  involved in the vibration described by internal coordinate  $q_n$  are non-zero. This led for the first time to mass-decoupled local vibrational modes  $\mathbf{a}_n$  which can be directly derived from normal vibrational modes  $\mathbf{d}_\mu$  and the force constant matrix  $\mathbf{K}$ , both being available after a standard frequency calculation. Fig. 3 illustrates the difference between a normal and a local mode for naphthalene.

$$\mathbf{a}_n = \frac{\mathbf{K}^{-1} \mathbf{d}_n^{\dagger}}{\mathbf{d}_n \mathbf{K}^{-1} \mathbf{d}_n^{\dagger}} \quad (15)$$

For each local mode  $\mathbf{a}_n$  the corresponding local mode frequency  $\omega_n^a$

$$(\omega_n^a)^2 = \frac{1}{4\pi^2 c^2} k_n^a G_{nn} \quad (16)$$

and the corresponding local mode force constant  $k_n^a$

$$k_n^a = \mathbf{a}_n^{\dagger} \mathbf{K} \mathbf{a}_n = (\mathbf{d}_n \mathbf{K}^{-1} \mathbf{d}_n^{\dagger})^{-1} \quad (17)$$

can be calculated via Eq. (16) and Eq. (17), respectively.

Local mode force constants, contrary to normal mode force constants are independent of the choice of the coordinates used to describe the molecule in question.<sup>137,146,147</sup> They are sensitive to differences in the electronic structure (e.g., caused by changing a substituent), and because they are, in contrast to frequencies, independent of the atomic masses, they capture pure electronic effects. In their landmark paper, Zou and Cremer<sup>148</sup> proved that the local stretching force constant  $k_n^a(\text{AB})$  reflects the intrinsic strength of the bond/interaction between two atoms A and B being described by an internal coordinate  $q_n$ . We have successfully applied local stretching force constants for the characterization of covalent bonds<sup>118,120,137,148–152</sup> and weak chemical interactions such as halogen bonds,<sup>117,153–157</sup> chalcogen bonds,<sup>158–160</sup> pnictogen bonds,<sup>161–163</sup> tetrel bonds,<sup>119</sup> and hydrogen bonds,<sup>164–172</sup> as well as so-called  $\pi$ -hole interactions.<sup>173</sup> Replacing the calculated vibrational frequencies in Eq. (16) with measured fundamental frequencies leads to experimentally based local mode force constants<sup>121</sup> which include anharmonicity effects which are not captured by calculated harmonic force constants.<sup>165,166</sup> This important feature makes LMA attractive to the experimental vibrational spectroscopists.

For the comparison of larger sets of  $k^d$  values, the use of a relative bond strength order BSO  $n$  is more convenient. Both are connected according to the generalized Badger rule derived by Cremer, Kraka and co-workers,<sup>79,137</sup> via the following power relationship:

$$BSO\ n = a(k^d)^b \quad (18)$$

The constants  $a$  and  $b$  in Eq. (18) are calculated from the  $k^d$  values of two reference compounds with known BSO  $n$  values and the requirement that for a zero force constant the corresponding BSO  $n$  value is zero. For example, for CC bonds suitable references are ethane and ethylene with bond orders  $n = 1$  and  $n = 2$ , respectively.<sup>150</sup> In the case of more complex bonding situations, e.g., metal-ligand bonding, guidance by Mayer bond orders<sup>174–176</sup> can be utilized.<sup>177</sup>

### 3 Applications

In the following three examples are discussed (1) Au-catalyzed[3,3]-Sigmatropic Rearrangement of Allyl Acetate, (2) Re-catalyzed CO<sub>2</sub> cycloaddition to epoxides (3)  $\alpha$ -ketoamide inhibitor for SARS-CoV-2 main protease. For each reaction, a reaction movie following the geometrical changes of the RC along the reaction parameter  $s$  from entrance to exit channel is included in the Supporting Materials, facilitating the discussions.

#### 3.1 Au-Catalyzed[3,3]-Sigmatropic Rearrangement of Allyl Acetate

Homogenous gold catalysis has attracted a lot of attention in the past two decades because it offers a large variety of organic transformations under mild reaction conditions and with high yields,<sup>178–182</sup> in part due to its unique relativistic properties,<sup>183–185</sup> leading to special gold-bonding features<sup>186–188</sup> determining its color.<sup>189</sup>

In particular cationic gold complexes efficiently activate intra- or intermolecularly CC, CN, or CO multiple bonds for a nucleophilic attack.<sup>190–194</sup> Au[III] catalysts can be considered as hard Lewis acids with a higher oxophilic character, being useful when d-holes are needed,<sup>190,195–197</sup> Au[I] species are soft Lewis acids with high carbophilic character and high affinity to coordinate with carbon  $\pi$ -systems.<sup>33,192,193,198–200</sup> Both Au[I] phosphine complexes and Au[I] complexes with heterocyclic carbenes (NHC) ligands<sup>201,202</sup> are applied where the latter display a broader range of versatility and regio-selectivity.<sup>203–207</sup>

We have studied both Au[I]-phosphine and Au[I]-NHC complexes in a comprehensive study of the Au-catalyzed[3,3]-sigmatropic Claisen Rearrangement of Allyl Acetate.<sup>103</sup> In the following the main results and highlights of this work are featured, demonstrating how URVA works and what we can expect. Fig. 4 shows the Non-catalyzed (R1), Au[I]-phosphine catalyzed (R2), and Au[I]-NHC (R3) catalyzed Claisen rearrangement of allyl acetate discussed in this article. In Table 1 the energetics of the three reactions are summarized and in Fig. 5 the reaction path curvature profiles of the three reactions are presented. Reaction movies following the evolution of the RC along the reaction path are provided for both the non-catalyzed reaction R1 and the two steps of the catalyzed reactions R2 and R3 in the Supporting Materials: videos M1 – M5.

Although the non-catalyzed reaction R1 is symmetry-allowed it has a relatively high barrier height of 37.4 kcal/mol limiting its usefulness for synthesis. The activation energies for the catalyzed reactions proceeding in two steps (see Fig. 4) are considerably lower;  $\Delta E^a = 8.8$  kcal/mol for the first and 4.2 kcal/mol for the second step of reaction R2 and 14.5 kcal/mol for the first step and 1.9 kcal/mol for the second step of reaction R3, respectively, see Table 1. This clearly shows the overall drastic effect of the gold-catalyst.

Mechanistic details about the factors which cause the high barrier of reaction R1 and how the catalyst supports the rearrangement can be obtained from the curvature profiles shown in Fig. 5. The pre-chemical phases 1 and 2 of reaction R1 (Fig. 5(a)) are characterized by the rotation of methyl groups and the acetate unit, and phase 3 by a pseudo-rotation of the 6-membered ring reducing the distance between the  $C_b$  and  $O_b$  atoms, which are forming a new bond (see reaction video M1, Supporting Materials).  $C_bO_b$  bond formation (red line) starts to contribute to the reaction path curvature already in phase 2 with a resisting component stretching to the start of phase 7. The  $C_aO_a$  bond cleavage starts in phase 5 with a supportive dominating contribution to curvature peak K3 (blue line). Phase 6, containing the TS is characterized by a smaller curvature peak K4. It is interesting to note that the RC adapts a boat form at the TS with  $C_aO_a$  and  $C_bO_b$  distances close to 2.1 Å. Both, the  $C_aO_a$  and the  $C_bO_b$  bonds are resisting a further change in this phase (see reaction video M1, Supporting Materials), indicating the situation of a hidden intermediate,<sup>78</sup> i.e., the possibility to break up the reaction in this area into two steps with lower activation energies, e.g., with a catalyst that transforms the TS of the non-catalyzed reaction into a stable intermediate (Fig. 4). In Phase 7, leading to the large curvature peak K5, the formation of the new  $C_bO_b$  bond is finalized. Phases 8–10 are characterized by six-membered ring pseudo-rotations as well as a final rotation of acetate methyl-group. In summary, the most important curvature peaks are K3 before the TS (breakage of the  $C_aO_a$  bond), K4 close to the TS (boat form of the RC with equal  $C_aO_a$  and  $C_bO_b$  bond lengths), and K5 after the TS (finalization of  $C_bO_b$  bond formation).

Fig. 5 (b,c) shows the curvature diagrams for the gold catalyzed reaction R2 which proceeds contrary to the non-catalyzed reaction R1 in two steps (see also videos M2 and M3, Supporting Materials). The first step starts from the  $\pi$ -bonded complex with the gold attached to the  $C_cC_b$  double bond of the allyl acetate and ends with the formation of an intermediate  $\sigma$ -bonded complex Au(I) complex with both the  $C_aO_a$  to be broken still intact and the new  $C_bO_b$  bond formed, thus resembling the TS of the non-catalyzed reaction. The energy consuming breakage of the  $C_aO_a$  bond determining the high barrier of reaction R1 is replaced with a less energy consuming loosening of the Au $C_b$  interaction. In addition, the Au atom pushes the  $C_b$  atom closer to the  $O_b$  atom (see reaction video M2, Supporting Materials) and in this way mediates the formation of the new  $C_bO_b$  bond which occurs like in reaction R1 after the TS. This explain the drastic drop in the activation energy from 37.4–8.8 kcal/mol. Since the formation of the Au- $\sigma$  complex is slightly endothermic by 0.7 kcal/mol, in

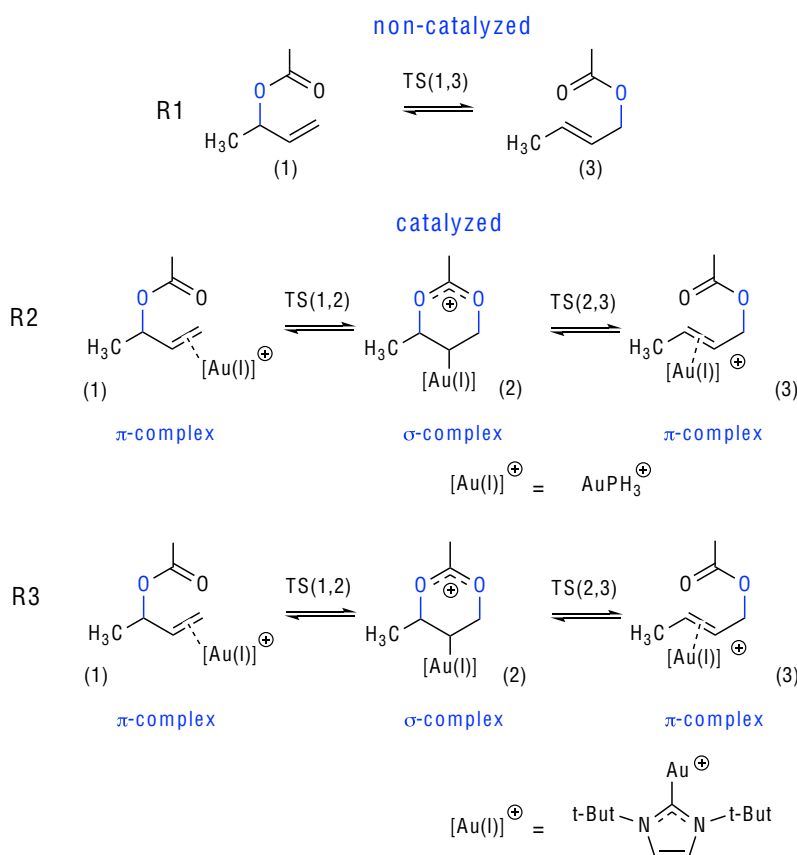


**Fig. 4** Non-catalyzed (**R1**), Au(I)-phosphine catalyzed (**R2**), and Au(I)-NHC (**R3**) catalyzed Claisen rearrangement of allyl acetate.

**Table 1** Activation energy  $\Delta E^{\ddagger}$ , activation enthalpy  $\Delta H^{\ddagger}$ , reaction energy  $\Delta E_R$  and reaction enthalpy  $\Delta H_R$  (kcal/mol) for reactions **R1** - **R3**. The values of the reaction second steps are given relative to the second step reactant. B3LYP/6-31 + G(d,p)/SDD(Au) level of theory.

Reaction	First step				Second step			
	$\Delta E^{\ddagger}$	$\Delta E_R$	$\Delta H^{\ddagger}$	$\Delta H_R$	$\Delta E^{\ddagger}$	$\Delta E_R$	$\Delta H^{\ddagger}$	$\Delta H_R$
<b>R1</b>	37.4	-0.6	35.6	-0.4				
<b>R2</b>	8.8	0.7	8.3	1.6	4.2	-2.3	3.0	-3.5
<b>R3</b>	14.5	7.9	13.9	8.6	1.9	-6.4	0.9	-6.9

Source: Freindorf, M., Cremer, D., Kraka, E., 2017. Gold(I)-assisted catalysis - A comprehensive view on the [3,3]-sigmatropic rearrangement of allyl acetate. Mol. Phys. 116, 161-630.

Step 2 the regeneration of a stable Au(I)- $\pi$ -complex occurs via establishing a new AuC<sub>*α*</sub> interaction (phase 2, green line) which simultaneously weakens the C<sub>*α*</sub>O<sub>*α*</sub> bond, supporting its cleavage (phase 2, blue line) which now requires only 4.2 kcal/mol.

**Fig. 5** (d,e) displays the curvature diagrams for reaction **R3** (see also videos M4 and M5, Supporting Materials). The overall curvature pattern of reactions **R2** and **R3** are the same, i.e., both Au(I) catalysts follow the same mechanism, despite the fact that later is a weaker Lewis acid, which is reflected in the activation energy of 14.5 kcal/mol being 5.7 kcal/mol higher than that of reaction **R3**. On the other hand, the activation energy of the second step is 2.3 kcal/mol lower and the reaction is more exothermic. There are two major difference in the curvature profiles of the two reactions concerning rotations. K1 in the first step of reaction **R2** results from PH<sub>3</sub> rotations and K4 in step two resulting from rotations of methyl substituent of C<sub>*α*</sub> is also more pronounced in reaction **R2** (see M4, Supporting Materials). The bulky t-but NHC substituents do not play any significant mechanistic role because of the structural arrangement of the NHC perpendicular to the plane of the 1,3-acetoxonium moiety as has been previously suggested.<sup>208</sup>

In summary, the URVA analysis shows how the Au(I) catalyst breaks up the non-catalyzed rearrangement into two steps by acting as a *chameleon*, e.g., easily switching between Au(I)- $\pi$  and Au(I)- $\sigma$  complexation. The catalytic action of the Au(I) catalyst of allyl acetate is due to (1) the formation of a stable  $\sigma$ -bonded intermediate avoiding to start with an energy-consuming breakage of

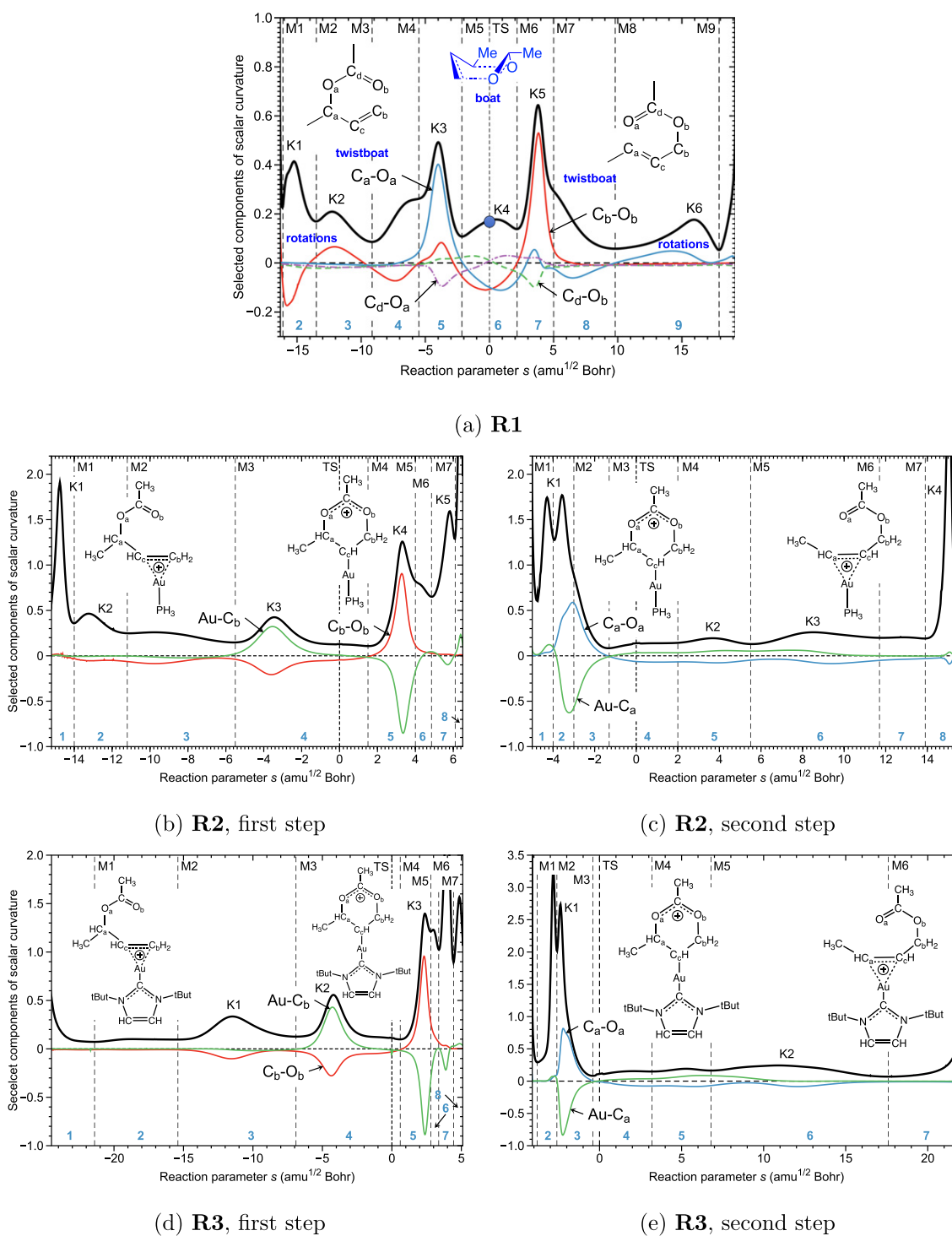


**Fig. 5** Scalar reaction curvature profile (solid black line) as a function of the reaction path parameter  $s$  and its decomposition into the most important components (colored lines) for the non-catalyzed reaction **R1** (a); for the two steps of catalyzed reaction **R2**, (b) and (c); and the two steps of catalyzed reaction **R3**, (d) and (e). The borders of the reaction phases are indicated by vertical dashed lines at curvature minima M1, M2, M3, etc. The reaction phases are indicated by blue numbers. Curvature maxima are given as K1, K2, K3, etc. The TS at  $s = 0 \text{ amu}^{1/2} \text{ Bohr}$  is also indicated by a vertical dashed line. B3LYP/6-31 + G(d,p)/SDD(Au) level of theory. Reprinted with permission from Freindorf, M., Cremer, D., Kraka, E., 2017. Gold(I)-assisted catalysis - A comprehensive view on the [3,3]-sigmatropic rearrangement of allyl acetate. *Mol. Phys.* 116, 611–630. Copyright 2020 from Taylor & Francis.

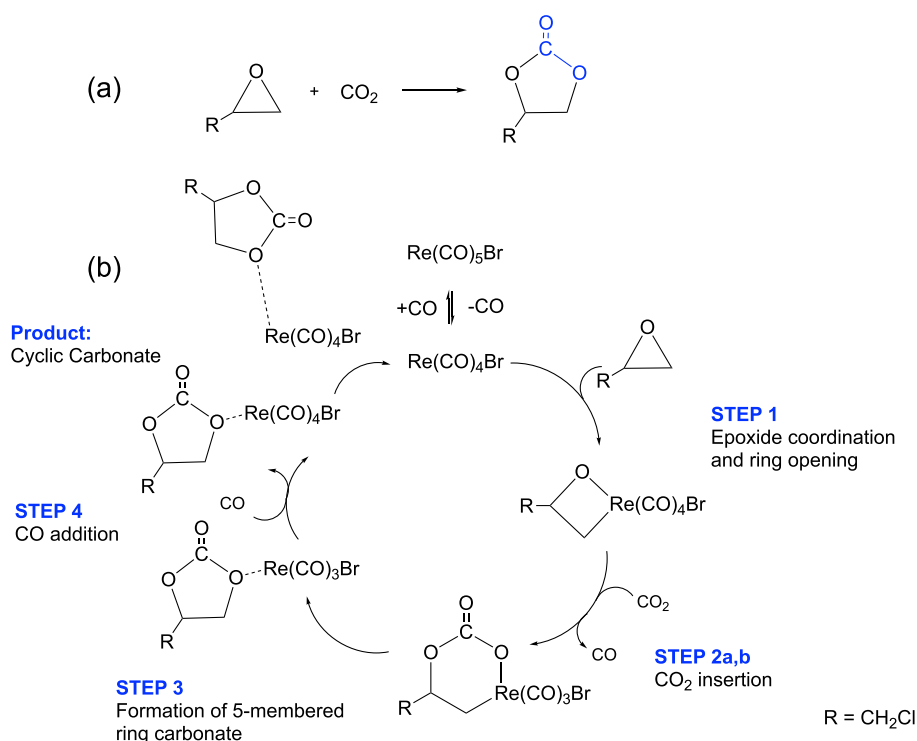


**Fig. 6** (a) Reaction scheme for the cycloaddition of CO<sub>2</sub> to a mono-substituted epoxide. (b) Catalytic cycle of the Re-catalyzed CO<sub>2</sub> cycloaddition to epichlorohydrin discussed in this work. Reproduced from Guo, C.H., Song, J.Y., Jia, J.F., Zhang, X.M., Wu, H.S., 2010. A DFT study on the mechanism of the coupling reaction between chloromethyloxirane and carbon dioxide catalyzed by Re(CO)<sub>5</sub>Br. *Organometallics* 29, 2069–2079.

the C<sub>a</sub>O<sub>a</sub> bond; (2) simplification of the ring pseudo-rotation, i.e., no need to bring the RC into a boat form and (3) the assistance of gold with the breaking and forming of the CO bonds.

### 3.2 Re-Catalyzed CO<sub>2</sub> Cycloaddition to Epoxides

The environmental concentration of CO<sub>2</sub> has been dramatically increased over the last decades, contributing to global warming.<sup>209</sup> The anthropogenic emission of CO<sub>2</sub> exceed now 36 Gt and due to the growing demand for energy is expected to increase even further by 25%–90% in the next decade.<sup>210</sup> A variety of new technologies are under development to reduce anthropogenic CO<sub>2</sub> emissions; one possible pathway, Carbon Capture and Utilization has recently attracted a lot of attention,<sup>211,212</sup> in particular the synthesis of cyclic carbonates from CO<sub>2</sub> cycloaddition to epoxides, sketched in Fig. 6(a)<sup>213–218</sup> Organic cyclic carbonates have a broad range of applications as high boiling point green polar aprotic solvents or electrolytes in Li-ion batteries, serving as monomer for polycarbonates and polyurethanes synthesis, intermediates for the manufacturing of pharmaceuticals and many other fine chemicals just to name a few.<sup>219</sup>

In the following we present a pilot study on the Re-catalyzed CO<sub>2</sub> cycloaddition to epichlorohydrin (chloromethyl oxirane) shown in Fig. 6(b) focusing on how URVA can unravel valuable mechanistic features for the optimization and redesign of this process as well as providing useful new insights for the use of this greenhouse gas as chemical feedstock as better alternative to its non-reactive sequestration. Re(CO)<sub>5</sub>Br-catalyzed coupling of epoxides with supercritical CO<sub>2</sub> was first suggested in 2005<sup>220</sup> and in 2010 theoretically investigated by Guo and co-workers<sup>221</sup> for the coupling of epichlorohydrin and CO<sub>2</sub> and providing an overall view of the energetics and the catalytic cycle shown in Fig. 6(b). In the following we show how URVA can add valuable mechanistic details with regard to the specific role of the catalyst mediating the bond forming/breaking processes.

An activation energy ΔE<sup>d</sup> of 60.4 kcal/mol (see Table 2) makes the direct cycloaddition shown in Fig. 6(a) unattractive for practical use. The ΔE<sup>d</sup> values for the five steps of our model catalytic cycle are ranging from 37.6 kcal/mol to 0.7 kcal/mol (see Table 2) providing evidence that the Re catalysts works in the right direction, i.e., substantially lowering the energy barrier. In order to learn more about the mechanistic details we followed the same strategy as in the previous example, we first focused on the URVA analysis of the non-catalyzed reaction in order to identify the chemical events which contribute to the large energy barrier (see Fig. 7), followed by the URVA analysis of each step of the catalytic cycle (see Fig. 8) focusing on how the Re atom mediates the cycloaddition. The corresponding reaction movies M6 - M11 can be found in the Supporting Materials.

**Table 2** Activation energy  $\Delta E^a$ , activation enthalpy  $\Delta H^a$ , reaction energy  $\Delta E_R$  and reaction enthalpy  $\Delta H_R$  (kcal/mol) of the Re catalyzed transformation of  $\text{CO}_2$ . The energy values in each reaction step are relative to the reactant of this reaction step. B3LYP/6–31 G(d,p)/SDD(Re) level of theory

	Energy		Enthalpy	
	$\Delta E^a$	$\Delta E_R$	$\Delta H^a$	$\Delta H_R$
Non-catalyzed	60.4	– 14.7	58.7	– 13.1
Re-catalyzed				
Step 1	37.6	24.7	35.8	23.8
Step 2	6.6	5.7	6.0	5.9
Step 3	13.3	8.5	12.7	8.6
Step 4	15.5	– 36.9	14.7	– 35.0
Step 5	0.7	– 30.4	– 0.8	– 30.7

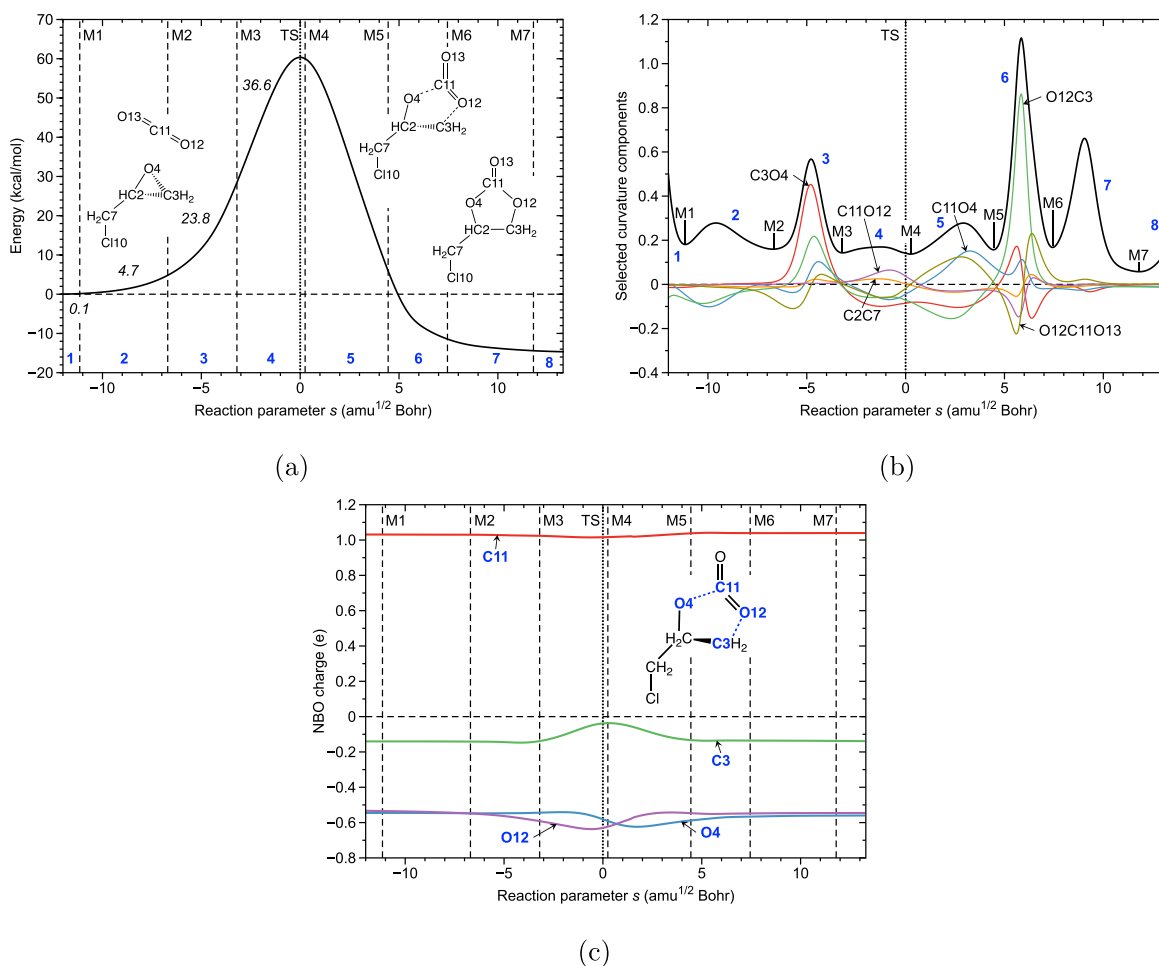


**Fig. 7** Non-catalyzed reaction between  $\text{CO}_2$  and epichlorohydrin. (a) Energy profile, the energy contribution to the total activation energy of each phase (in kcal/mol) is shown; (b) Scalar reaction curvature profile (solid black line) as a function of the reaction path parameter  $s$  and its decomposition into selected components (colored lines); (c) NBO atomic charges of selected atoms along the reaction path. B3LYP/6–31G(d,p) level of theory.

There are two possible causes for the high barrier of the direct cycloaddition (1) ring-opening of the epoxide, i.e., breakage of one epoxide CO bond and (2) activation of the inert  $\text{CO}_2$ , requesting the elongation of one carbon dioxide CO bond and the bending of the molecule, or a combination of both. Whereas the energy profile shown in Fig. 7(a) cannot answer this question, the

reaction path curvature profile shown in Fig. 7(b) provides these insights. The reaction is composed of eight phases, phase 4 including the TS. In phase 3 the major chemical event contributing to the activation energy with 23.8 kcal/mol is the breakage of the epoxide bond C3O4 (red line) accompanied by the start of C3O12 (green line) and C11O4 (blue line) bond formation and the bending of the CO<sub>2</sub> molecule (olive line). In phase 4 with an energy contribution of 36.6 kcal/mol the elongation of the C11O12 carbon bond of CO<sub>2</sub> comes into play. The formation of the new C11O4 bond is finalized in phase 5 followed by the finalization of the C3O12 bond in phase 6 which is more difficult, because as shown in Fig. 7(c) both C3 and O12 are negatively charged and therefore have to overcome electrostatic repulsion. Phases 7 and 8 are characterized by the five-membered ring adjustments and rotations of the CH<sub>2</sub>Cl group.

Step 1, *Epoxide coordination and ring opening* (Fig. 8(a), reaction movie M7, Supporting Materials). This step starts from Re(CO)<sub>4</sub>Br being loosely coordinated with the epoxide (distance ReO = 2.3 Å). As reflected by the curvature diagram, the whole reaction proceeds via 7 distinct phases: In phase 2, the oxirane reorganizes with regard to the transition metal atom leading to a slight increase of the ReO distance and a decrease of the ReC<sub>a</sub> distance. The most distinct peak before the TS is found in phase 3 characterized by the simultaneous start of epoxide C<sub>a</sub>O bond breakage (blue line) and ReC<sub>a</sub> bond formation (green line) with a only a small contribution of the ReO bond (purple line) hindered by a resisting C<sub>b</sub>O bond (red line), which must lengthen. These interactions reflect a donation of the C<sub>a</sub>O bonding electron pair to an empty Re d-orbital which weakens the CO bonds and facilitates C<sub>a</sub>O bond breakage, reducing the barrier by 22.8 kcal/mol. In phase 4, which also contains the TS, the ReC<sub>w</sub>, ReO and C<sub>a</sub>O bonds resist further change (negative components, maximum values at the TS). In phase 5, C<sub>a</sub>O bond breakage is completed, the new ReO, ReC<sub>a</sub> bonds are finalized, and a four membered ring (4MR) is formed leading to an expansion of the coordination sphere of the Re atom from 5 to 7. Typical for a catalytic reaction, bond forming/breaking processes are stretched over several phases, in particular into the exit channel making them less cost intensive.

Step 2a, *CO<sub>2</sub> insertion, formation of a bicyclic structure* (Fig. 8(b), reaction movie M8, Supporting Materials). After loss of one CO ligand the metal complex prepares in Step 2a for the CO<sub>2</sub> insertion. The CO<sub>2</sub> coordinates to the metal via one oxygen atoms (O<sub>b</sub>) and the central C atom (C<sub>c</sub>) is attracted by the oxirane oxygen (O<sub>a</sub>). The metal coordination guides the reacting atoms in the right position, a process which stretches over the first 2 phases. In phase 3 the chemical processes start with a bending of the linear O = C = O and the formation of a biradicaloid structure. All major chemical events leading to the addition of CO<sub>2</sub> to the Re atom occur in phase 4, after the TS, i.e., they do not contribute to the small barrier of only 6.6 kcal/mol. In this important phase the new O<sub>a</sub>C<sub>c</sub> bond is formed and the ReO interactions adjust so that both O atoms are loosely coordinated to Re (ReO distance: 2.18 Å). The resulting complex possesses a somewhat strained bicyclic structure characterized by 7-coordinated Re atom with 18 electrons in its valence shell. This relaxes to a six-membered ring in the following step.

Step 2b *CO<sub>2</sub> insertion, formation of a six-membered ring* (Fig. 8(c), reaction movie M9, Supporting Materials) This step is characterized by the cleavage of the ReO<sub>a</sub> bond leading to a six-membered carboxylate ring (6MR) out of which the following catalyst migration and the formation of a five-membered (5MR) ring carbonate is facilitated. In the first 3 phases, the 4MR ring containing C<sub>a</sub> puckers moving the C<sub>a</sub>H bonds out of the mean ring plane, so that the ReO<sub>a</sub> bond slightly lengthens preparing for its cleavage starting in phase 4. The Re-Br bond is initially resisting and then supporting the bond cleavage. In phases 5 and 6 the 6MR adjusts to a distorted boat form with the keto group in one of the 4 hull positions to guarantee a larger internal ring angle.

Step 3 *Formation of a 5-membered ring carbonate* (Fig. 8(d), reaction movie M10, Supporting Materials) In this reaction the 6MR is transformed into a 5MR reducing the coordination number of Re to 5. This process requires the cleavage of the ReC<sub>a</sub> bond and the formation of a new bond between O<sub>b</sub> and C<sub>a</sub>. Phases 1 and 2 are dominated by puckering changes of the 6MR. In phase 3, the cleavage of the ReC<sub>a</sub> bond starts and is stepwise continued in phases 4, 5, and 6, (red line, curvature diagram). The formation of the C<sub>a</sub>O<sub>b</sub> bond also starts in phase 3 and it is finalized in phase 5 stretching over almost 25 s units driving all other bond length changes. Phases 6 and 7 are characterized by conformational changes of the 5MR and the final adjustment of the ReC<sub>a</sub> and ReO<sub>b</sub> distances.

Step 4 *CO addition* (Fig. 8(e), reaction movie M11, Supporting Materials) The final step before carbonate elimination and catalyst regeneration is the addition of CO to the Re atom. This reaction which stretches over 8 phases has a small barrier of less than 1 kcal/mol determined by small conformational changes taking place in phases 1–3 and the onset of ReC<sub>d</sub> bond formation (blue line) which is first resistant (most negative component value around the TS). The ReC<sub>d</sub> bond is finalized in phase 6 far out in the exit channel indicated by a large curvature peak. The resulting 4-chloromethyl-[1,3]dioxolane-2-one molecule is bound to the complex by weak electrostatic interactions between Re and O<sub>b</sub> as confirmed by an electron density analysis. Therefore, the final carbonate elimination and catalyst regeneration proceed without any barrier.

In summary, the key role of the Re-catalyst is to mediate and support the coupling of CO<sub>2</sub> and oxirane via the formation and cleavage of a series of ReC and ReO bonds, which in each of the different steps stretches over several reaction phases, and as such imply a series of small energy-saving changes rather than an abrupt change consuming a larger amount of energy. Another key feature is the ability of Re to easily change its coordination sphere thus facilitating the coupling reaction.

### 3.3 α-ketoamide Inhibitor for SARS-CoV-2 Main Protease

The topic of the third example is enzyme catalysis. Over the past decades, a lot of emphasis has been devoted to replace traditional chemical processes relying on heavy metal catalysts (often leading to toxic byproducts) with Nature's powerful way of producing environmentally pure compounds under eco-friendly conditions using enzymes as catalysts. Nature has designed over billions of years the most efficient catalysts accelerating chemical reactions under the physical conditions in which organisms live by more

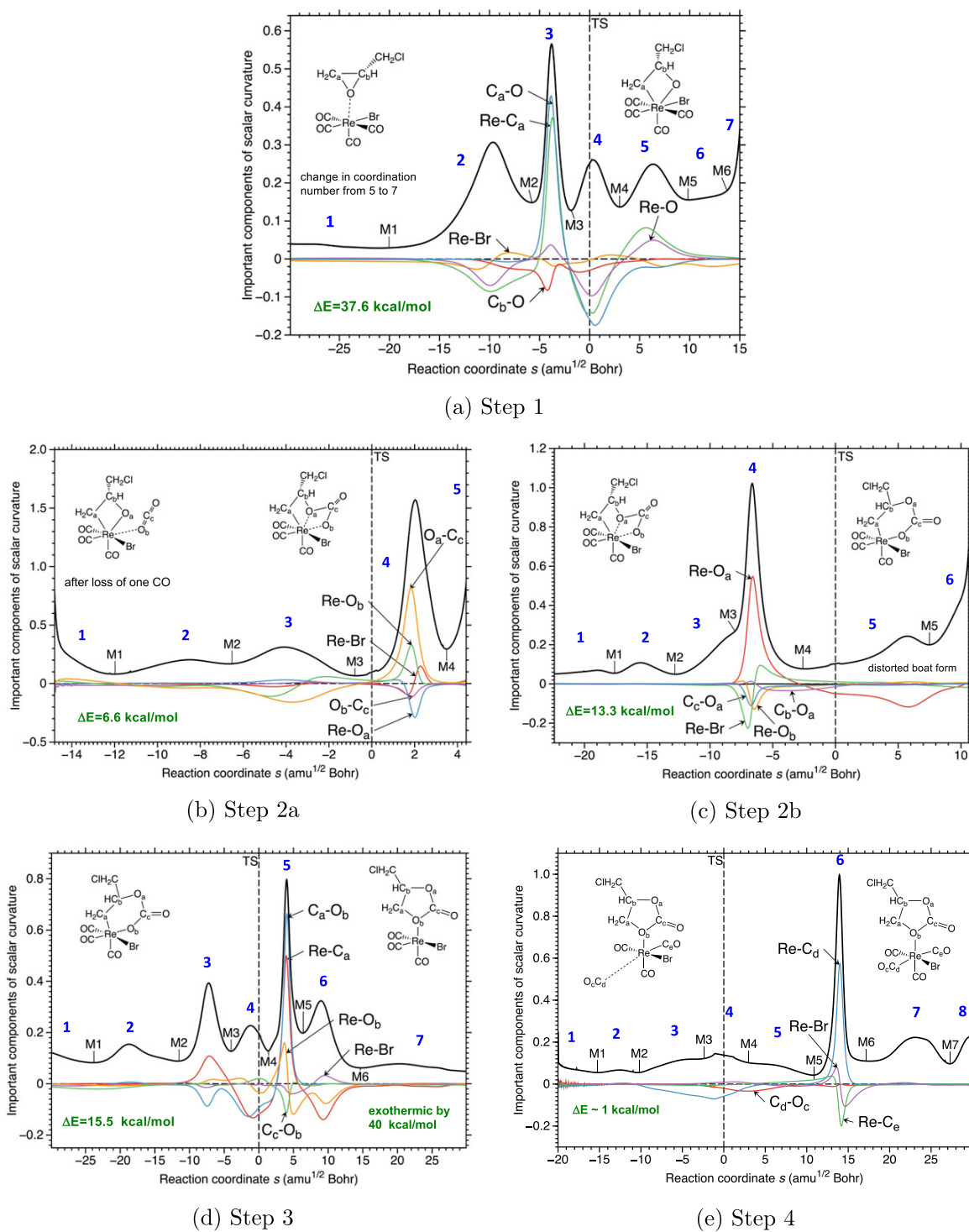


**Fig. 8** Scalar reaction curvature profile (solid black line) as a function of the reaction path parameter  $s$  and its decomposition into selected components (colored lines) for the  $\text{Re}(\text{CO})_4\text{Br}$ -catalyzed reaction between  $\text{CO}_2$  and epichlorohydrin. (a) Step 1; (b) Step 2a; (c) Step 2b; (d) Step 3; and (e) Step 4 of the catalytic cycle shown in Fig. 6(b). B3LYP/6-31G(d,p)/SDD(Re) level of theory.

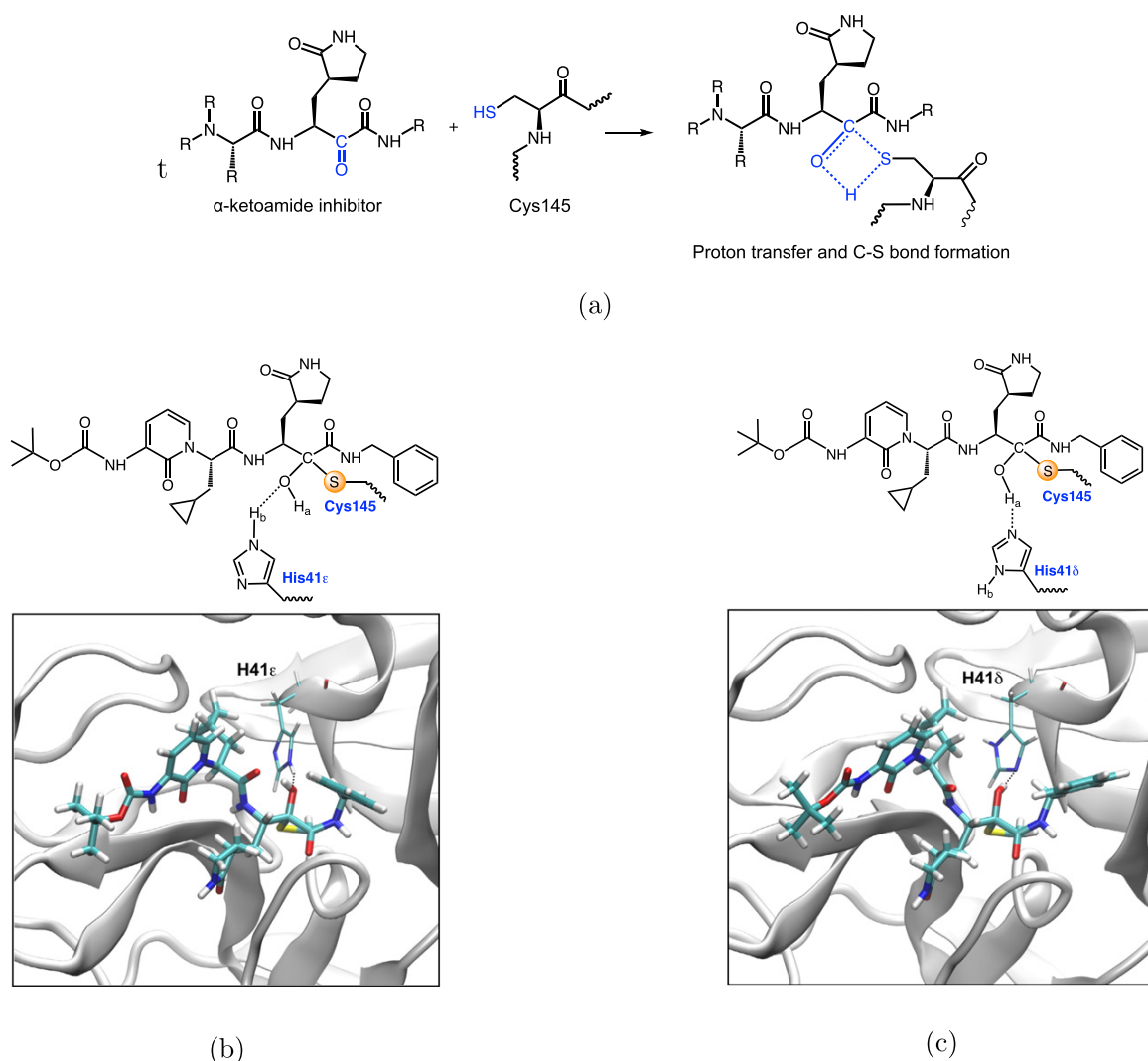


**Fig. 9** (a) One-step reaction between  $\alpha$ -ketoamide inhibitor and Cys145 of SARS-CoV-2M<sup>pro</sup>. (b)  $\alpha$ -ketoamide inhibitor after CS bond formation in the active site pocket of SARS-CoV-2M<sup>pro</sup> for the His41 $\epsilon$  protonation form, (c) for the His41 $\delta$  protonation form.

than a factor of  $10^{20,222-226}$  which has inspired the community to design so-called metalloenzymes combining Nature's efficiency with the robustness of man-made catalysts<sup>12,14,227,228</sup> or to create new artificial enzymes based on Nature's principle.<sup>10,11,229,230</sup> Whereas in this scenarios acceleration of the reaction rate is the major goal, there is another scenario frequently desired e.g., in drug design, i.e., to reduce the rate of an enzyme-catalyzed reaction or to completely prevent the reaction in an enzyme, which may lead to disease. In this scenario the catalyst works as an inhibitor, also called *negative catalyst*, which should not be confused with the term negative catalyst applied to enzyme-catalyzed reactions that do not follow the Bell-Evans-Polanyi principle,<sup>231,232</sup> which states that the driving force of a chemical reaction should be proportional to its activation energy.<sup>233</sup>

Since December 2019, the world has been suffering from a global pandemic, the coronavirus disease (COVID-19) caused by the highly contagious severe acute respiratory syndrome coronavirus 2 (SARS-CoV-2).<sup>234-237</sup> So far, more than 250 M cases and more than 5 M deaths have been reported worldwide.<sup>238</sup> Although the development of several vaccines against COVID-19 has slowed down the spread, the pandemic is still among us.<sup>239</sup> Many proteins in SARS-CoV-2 have been targeted for the design of new drugs or repurposing of known drugs<sup>240-243</sup> The main protease of SARS-CoV-2 (SARS-CoV-2M<sup>pro</sup>), a cysteine protease (CP) that takes part in the viral replication process has been one promising candidate,<sup>244-246</sup> in particular for the design of an  $\alpha$ -ketoamide inhibitor<sup>247</sup> that blocks the virus from replication.<sup>248-250</sup> A recent crystal structure of the inhibitor bound SARS-CoV-2M<sup>pro</sup><sup>251</sup> suggests that the  $\alpha$ -ketoamide inhibitor forms a CN bond with Cys145 of the virus, i.e., identifying the inhibitor as a covalent binder. Generally, covalent inhibitors have turned out to be more efficient and selective than their non-covalent counterparts, because they form covalent bonds with the proteins, which makes them attractive.<sup>252-254</sup> Most of the designs of covalent inhibitors

**Table 3** Activation energy  $\Delta E^{\ddagger}$ , activation enthalpy  $\Delta H^{\ddagger}$ , reaction energy  $\Delta E_R$  and reaction enthalpy  $\Delta H_R$  (kcal/mol) of the CS bond formation between  $\alpha$ -ketoamide inhibitor and SARS-CoV-2 main protease. The B3LYP/6-31G(d,p)/AMBER level of theory

	Energy		Enthalpy	
	$\Delta E^{\ddagger}$	$\Delta E_R$	$\Delta H^{\ddagger}$	$\Delta H_R$
Gas phase	40.3	7.2	38.4	8.8
Protein (His41 $\epsilon$ )	34.4	-6.8	33.0	-3.8
Protein (His41 $\delta$ )	31.4	-11.6	28.7	-10.6

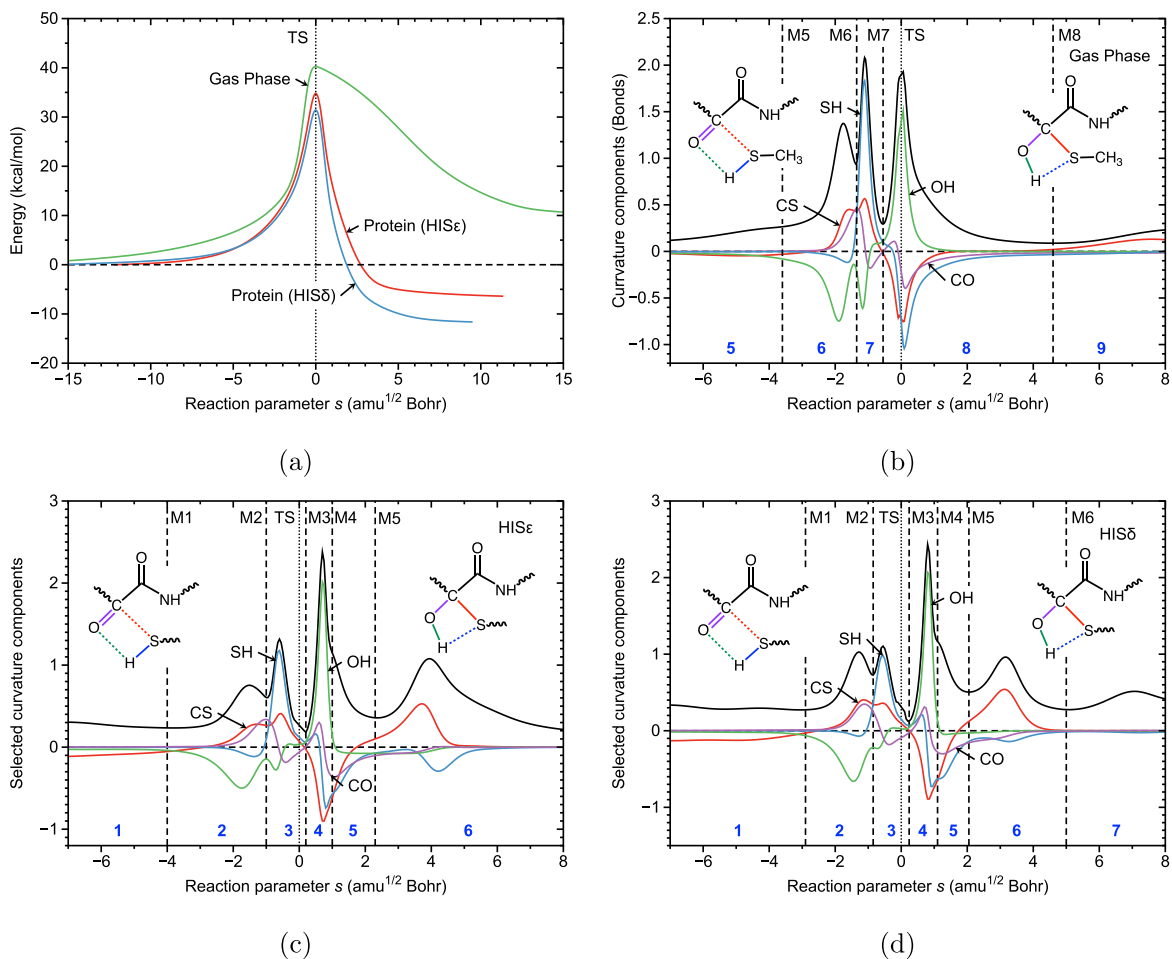


**Fig. 10** (a) Energy profiles for the one-step reaction between  $\alpha$ -ketoamide inhibitor and CH<sub>3</sub>-SH (gas phase) and Cys145 of SARS-CoV-2M<sup>pro</sup> (protein). (b) - (d) Scalar reaction curvature profile (solid black line) as a function of the reaction path parameter  $s$  and its decomposition into selected components (colored lines); (b) gas phase reaction, only reaction phases 5–9 are shown; (c) reaction in the protein with His41 $\epsilon$  protonation form; (d) reaction in the protein with His41 $\delta$  protonation form. Gas phase: B3LYP/6-31G(d,p) level of theory, protein: B3LYP/6-31G(d,p)/AMBER level of theory.

is so far based on experimental studies while computational research is still lacking behind. The major reason is following: non-covalent binding can be reasonably described with molecular dynamics (MD) computational protocols.<sup>255</sup> MD is a popular method in the drug design community, very fast but less accurate, because it is based on a classical molecular mechanics (MM) approach<sup>256–258</sup> treating the bonds of a molecule as springs while totally ignoring the electrons. Covalent binders need a more sophisticated description, in particular with regard to the description of the chemical bond being formed between inhibitor and

**Table 4** Bond length ( $\text{\AA}$ ), local mode force constant ( $\text{mDyn/\AA}$ ), and bond strength order for the reactant, TS and the product of the CS, SH, OH, CO, and NH bonds investigated in our study in the gas phase and in the protein. Gas phase: B3LYP/6–31G(d,p) level of theory, protein: B3LYP/6–31G(d,p)/AMBER level of theory

Bond	Reactant			TS			Product		
	R ( $\text{\AA}$ )	$k^2$ ( $\text{mDyn/\AA}$ )	BSO	R ( $\text{\AA}$ )	$k^2$ ( $\text{mDyn/\AA}$ )	BSO	R ( $\text{\AA}$ )	$k^2$ ( $\text{mDyn/\AA}$ )	BSO
Gas phase									
C-S	4.2291	0.014	0.015	2.7350	0.408	0.220	1.8746	1.962	0.760
S-H <sub>a</sub>	1.3495	4.035	0.752	1.8512	0.122	0.231	2.7113	0.108	0.222
O-H <sub>a</sub>	2.4720	0.003	0.066	1.0862	0.569	0.389	0.9683	7.958	0.945
C-O	1.2158	12.340	1.872	1.2952	6.805	1.249	1.4087	4.399	0.929
HIS $\epsilon$									
C-S	3.1082	0.153	0.101	2.2425	0.347	0.193	1.8624	2.158	0.819
S-H <sub>a</sub>	1.3527	4.062	0.753	1.5965	0.613	0.398	2.6982	0.224	0.284
O-H <sub>a</sub>	2.6142	0.070	0.192	1.3212	0.299	0.313	0.9730	7.620	0.931
C-O	1.2147	12.621	1.900	1.3054	7.575	1.343	1.4002	4.759	0.980
O-H <sub>b</sub>	1.9408	0.200	0.273	1.9696	0.157	0.252	2.0486	0.114	0.226
HIS $\delta$									
C-S	2.9231	0.186	0.118	2.1671	0.453	0.239	1.8458	2.264	0.850
S-H <sub>a</sub>	1.3544	4.051	0.753	1.5762	0.723	0.421	2.6410	0.297	0.312
O-H <sub>a</sub>	2.7224	0.067	0.189	1.3699	0.324	0.321	0.9750	7.773	0.937
C-O	1.2203	11.967	1.833	1.3158	6.792	1.247	1.4171	4.323	0.918
N-H <sub>a</sub>	1.9467	0.181	0.264	2.1457	0.165	0.256	1.8723	0.514	0.375

enzyme, e.g., offered by so-called hybrid quantum mechanics/molecular mechanics (QM/MM) methodologies, which combine accurate quantum chemical methods describing both nuclei and electrons with fast but less accurate MM approaches.<sup>259,260</sup> The inhibitor and a sufficiently large portion of the active site of the enzyme including the chemical bond to be formed are described with QM and the remainder of the protein with MM. However, this is not a black-box approach, and results may depend on the choice of the active site, level of theory used for the QM part and other approximations.<sup>226,261–268</sup>

In the following we present a combined URVA and LMA QM/MM study of the  $\alpha$ -ketoamide inhibitor inside SARS-CoV-2M<sup>pro</sup> focusing on (1) the mechanism of CS bond formation between the inhibitor and Cys145 of SARS-CoV-2M<sup>pro</sup> and (2) the assessment of the strength of this CS bond; following the same protocol we recently applied to the *Bacillus subtilis* chorismate mutase (BsCM) catalyzed Claisen rearrangement of chorismate to prephenate<sup>33</sup> (sketched in Fig. 1(c)), which forms an important part of the *shikimate* pathway controlling the synthesis of aromatic amino acids in the cells of fungi, bacteria and plants.<sup>269–271</sup>

The formation of the CS bond between the  $\alpha$ -ketoamide inhibitor and the side chain of Cys145 in SARS-CoV-2M<sup>pro</sup> was investigated in our study as a one-step reaction, in which the nucleophilic attack of cysteine on the C carbonyl atom of the inhibitor takes place synchronously with hydrogen migration from Cys145 to the carbonyl oxygen atom of the inhibitor (see Fig. 9(a)). The CS bond formation in the protein is influenced by the interaction with the His41 residue of SARS-CoV-2M<sup>pro</sup>, which is located in close proximity of the reaction site. There are two different protonation forms of His41 determining how it interacts; in His41 $\epsilon$  the interaction is via a hydrogen atom of the  $\epsilon$  nitrogen atom of the histidine imidazole ring (Fig. 9(b)) and in His41 $\delta$  via the lone pair of the  $\delta$  nitrogen atom of the histidine imidazole ring (Fig. 9(c)). Both possibilities were considered in our QM/MM study of the protein reaction and compared with the reaction in the gas phase, where the cysteine residue was modeled by CH<sub>3</sub>-SH.

The activation and reactions energies along with the activation and reaction enthalpies for the three reactions are reported in Table 3. According to Table 3 the activation energy  $\Delta E^{\ddagger}$  of the reaction in the gas phase has a value of 40.3 kcal/mol, which is energetically higher than the activation energies calculated in the protein (34.4 and 31.4 kcal/mol, for the His41 $\epsilon$  and His41 $\delta$  protonation forms, respectively). This indicates that the protein environment, in particular the His41 interaction supports CS bond formation. In the gas phase the reaction is endothermic with a reaction energy  $\Delta E_R$  of 7.2 kcal/mol, making it unfavorable. In contrast, the reaction in the protein becomes exothermic with reaction energies of  $-6.8$  and  $-11.6$  kcal/mol, for the His41 $\epsilon$  and His41 $\delta$  protonation forms, respectively. This shows the efficiency of the inhibitor establishing a chemical bond with SARS-CoV-2M<sup>pro</sup> being supposed to block the virus from replication. The corresponding enthalpy values in Table 3 reflecting thermal effects show the same trends.

In the next step we used URVA to explore the mechanistic details leading to a better understanding of what causes the decrease of the barrier in the protein and why the reaction becomes exothermic in the protein environment. Fig. 10(a) compares the energy profiles for the three reactions and Fig. 10(b–d) show the corresponding curvature profiles. The corresponding reaction movies M12 – M14 can be found in the Supporting materials.

### 3.3.1 Gas phase reaction

There are 9 distinct reaction phases. Phases 1–4 are uneventful preparation phases which are not in Fig. 10(b). Phase 6 is characterized by the start of CS bond formation (red line) and transformation of the carbonyl CO double bond of inhibitor into a single bond (purple line), both being supportive. Hydrogen migration involving the formation of the new OH bond (green line) and the cleavage of the SH bond (green line) are still resisting. The formation of the new OH bond starts in phase 6. Whereas OH bond formation is still

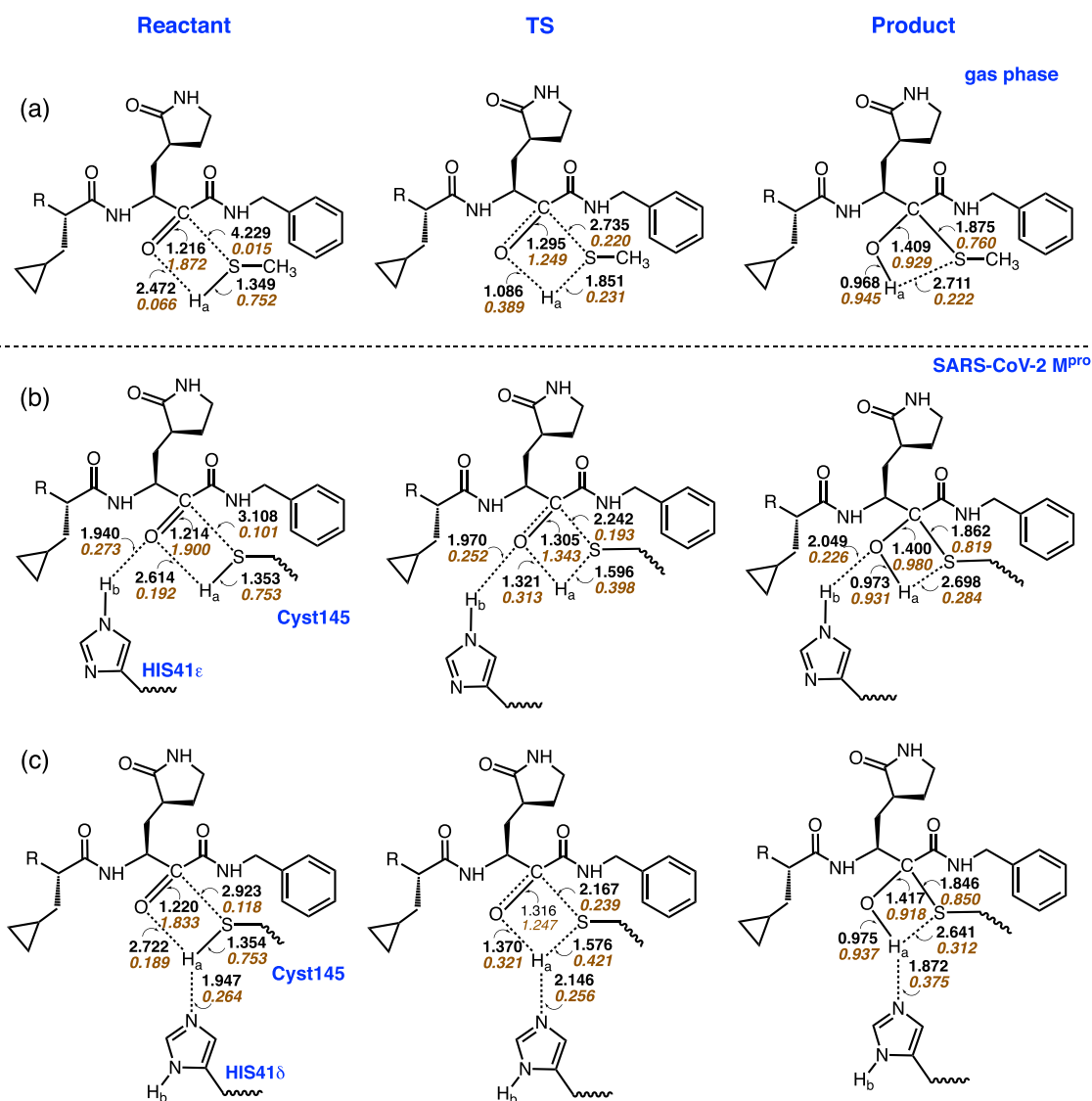


**Fig. 11** Chemdraw sketches of the reactant complex, TS, and product complex for gas phase and protein. Bond length in Å (black numbers) and BSO  $n$  values (brown, italic numbers) are given for all bonds/interactions involving the proton shift and CS bond formation. (a) Gas phase reaction, (b) His41 $\epsilon$  protein reaction, and (c) His41 $\delta$  protein reaction. Gas phase: B3LYP/6–31G(d,p) level of theory, protein: B3LYP/6–31G(d,p)/AMBER level of theory.

resting in phase 7, SH bond cleavage becomes supportive and dominating the large curvature peak. In phase 8 including the TS, finalization of OH bond formation becomes the dominating event accompanied by the finalization of CS bond formation as well as SH bond cleavage and CO bond adjustment leading to a large curvature peak located at the TS, i.e., all these events account for the barrier.

### 3.3.2 Protein reaction

As revealed by the curvature pattern shown Fig. 10(c) and 10(d), the overall reaction mechanism in the protein is similar to that in the gas phase. However, there are two important differences. For both the His41 $\epsilon$  and the His41 $\delta$  protonation form the large curvature peak connected with the finalization of OH bond as well as SH bond cleavage and CO bond adjustment have been moved into phase 4 after the TS which is contained in phase 3, i.e., these events do not longer contribute to the energy barrier, explaining the lower activation energies in the protein. Whereas in the gas phase CS bond formation is completed synchronously with OH bond formation (see phase 8) in the protein the CS bond formation is finalized in a subsequent phase (phase 6, read line, supporting) reflecting the final adjustment in the binding pocket.

URVA was complemented with LMA performed at the stationary points, i.e., reactant complex, TS, and product complex for each of the three reactions to assess and compare the strength of the formed and cleaved bond in gas phase and protein. In

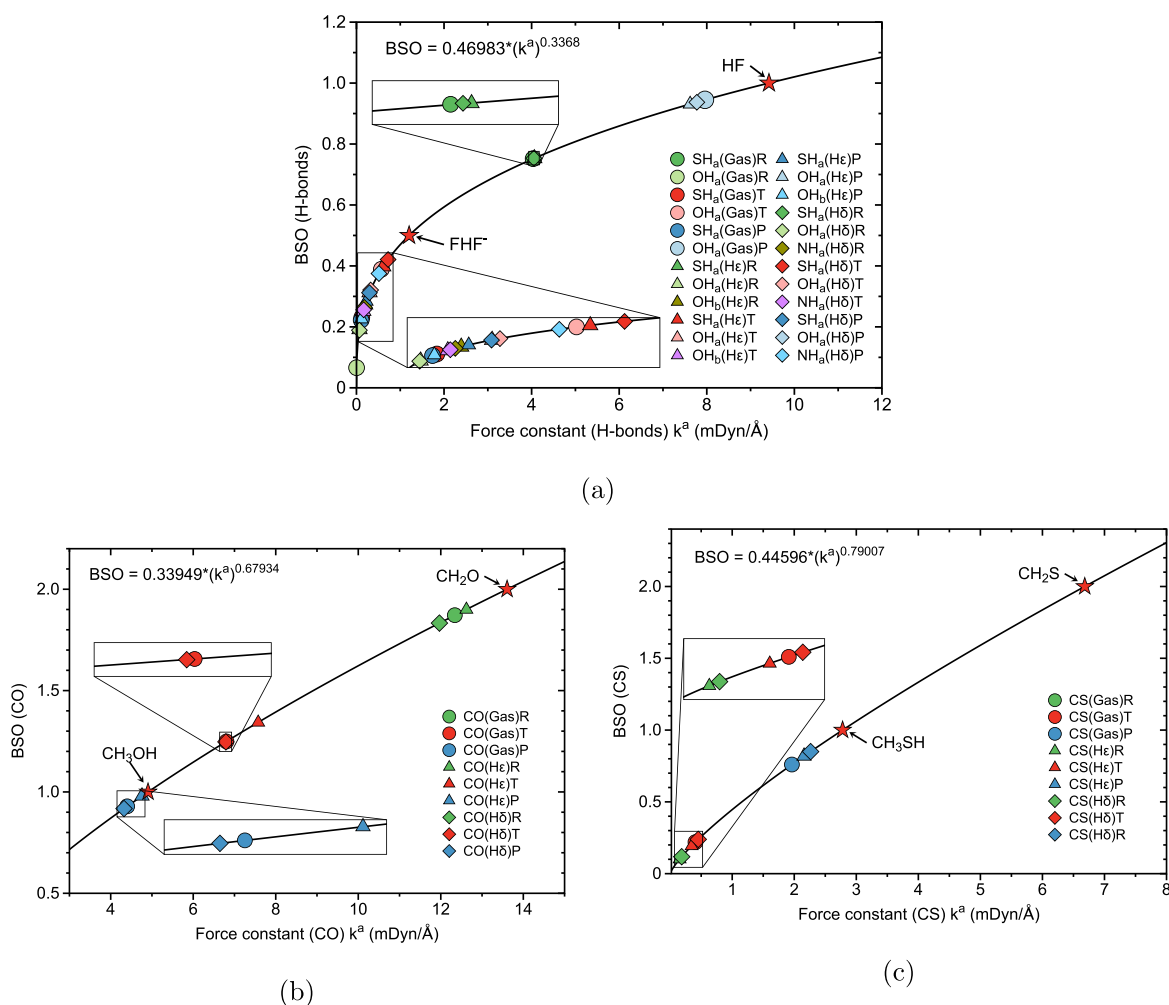


**Fig. 12** Power relationship between constant  $k^a$  and bond strength order BSO  $n$  calculated via Eq. (18). (a) For hydrogen bonds, (b) for CO bonds, (c) for the CS bonds for the gas phase (Gas), and protein calculations (H $\epsilon$ , H $\delta$ ). Symbols R, T, and P denote reactant complex, TS, and product complex, respectively. Gas phase: B3LYP/6–31G(d,p) level of theory, protein: B3LYP/6–31G(d,p)/AMBER level of theory.

addition to local mode force constants  $k^a$  we also calculated the corresponding strength order BSO  $n$  via Eq. (18) which provide a more intuitive measure of bond strength. For the OH and SH bonds we used as references FHF $^-$  (BSO  $n = 0.5$ ,  $k^a(\text{FH}) = 1.203$  mDyn/Å) and HF (BSO  $n = 1.0$ ,  $k^a(\text{FH}) = 9.420$  mDyn/Å), for CO bonds CH $_3$ OH (BSO  $n = 1.0$ ,  $k^a(\text{CO}) = 4.905$  mDyn/Å) and CH $_2$ O (BSO  $n = 2.0$ ,  $k^a(\text{CO}) = 13.607$  mDyn/Å), and for CS bonds CH $_3$ SH (BSO  $n = 1.0$ ,  $k^a(\text{CS}) = 2.779$  mDyn/Å) and CH $_2$ S (BSO  $n = 2.0$ ,  $k^a(\text{CS}) = 6.682$  mDyn/Å).

In Table 4 and Fig. 11 the corresponding bond lengths R, local mode force constants  $k^a$  and BSO  $n$  values for the CS, SH, OH, CO, and NH bonds at the stationary points are summarized for each reaction investigated in this work. Fig. 12 presents the corresponding  $k^a$  versus BSO  $n$  power relationships; Fig. 12(a) for all OH and SH bonds, Fig. 12(b) for all CO bonds and Fig. 12(c) for all CS bonds including the reference molecules providing a more holistic view.

Most important is the CS bond. Its formation contributes to the activation energy and to the final stabilization of the inhibitor-protein complex, a stronger CS bond will block the replications of virus more efficiently. The initial CS interaction is the weakest the gas phase with as reflected by a BSO  $n$  value of 0.0015, caused by the long CS distance of 4.229 Å (see Table 4 and Fig. 11). In the protein, caused by space confinement in the active site, the CS distance is considerably reduced to a value of 3.108 Å in His41 $\epsilon$  and 2.9231 Å in His41 $\delta$ . This leads to a somewhat stronger interaction (BSO  $n$  values of 0.101 and 0.118 for the H41 $\epsilon$  and H41 $\delta$ , respectively) from the start leading to a smaller barrier. In the final inhibitor-protein complex His41 $\delta$  has the strongest CS bond with a BSO value of 0.850 compared with BSO  $n$  values of 0.819 for His41 $\epsilon$  and 0.760 for the gas phase reaction.

In addition to CS bond formation the reaction barrier also depends on the proton migration, which involves SH breakage and OH $_a$  formation both starting before the TS. As reflected by the data in Table 4 and Fig. 11 there is no significant difference between the three reactions, the same holds for the SH $_a$  and OH $_a$  bond strengths in the final inhibitor-protein complex. In each case the

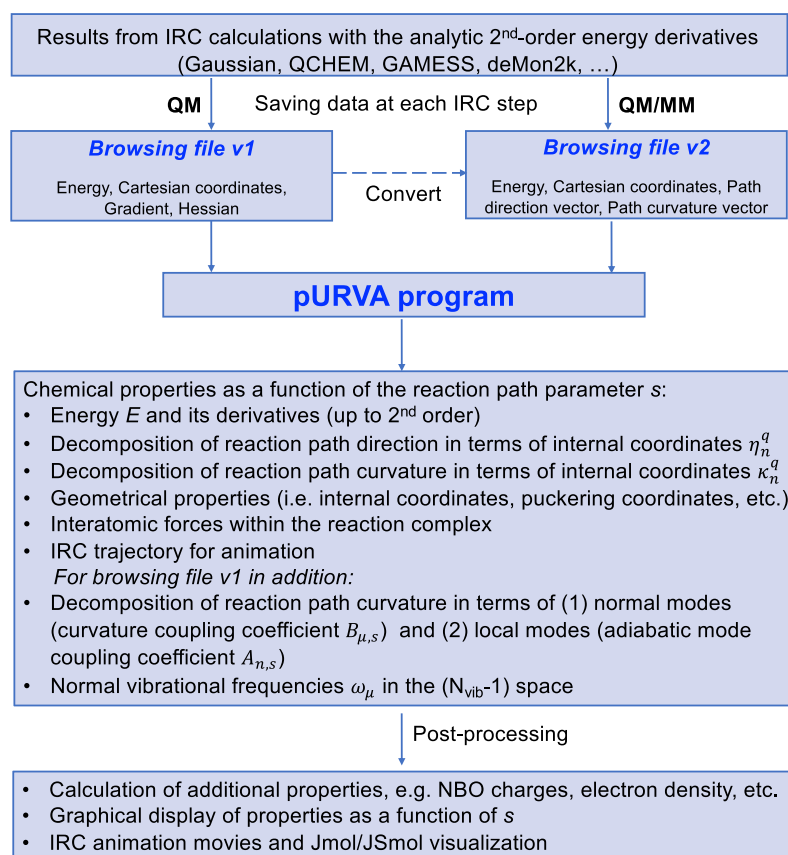


**Fig. 13** Flowchart of the pURVA software. Reprinted with permission from Kraka E, Zou W, Tao Y, Freindorf M. Exploring the Mechanism of Catalysis with the Unified Reaction Valley Approach (URVA) – A Review. *Catalysts*. 2020;10:691, copyright 2021 from MDPI

covalent SH bond in the reactant complex (BSO  $n$  values in the 0.753 range) changes to a weak chemical interaction in the product complex (BSO  $n$  values ranging from 0.222 to 0.312). The OH<sub>a</sub> bond is changing in the opposite way, i.e., the weak chemical OH<sub>a</sub> interaction in the reactant (BSO  $n$  values from 0.066 to 0.189) transforms into a covalent OH<sub>a</sub> bond in the final product (BSO  $n$  values ranging from 0.918 to 0.945). The change of the keto CO bond from double to single bond is comparable for the three reactions reflected by BSO  $n$  values in the range of 1.872–1.900. It is interesting to note that the CO double bond in His41δ is the longest and weakest among the three bonds, ( $R = 1.220 \text{ \AA}$  and BSO  $n = 1.833$ ).

The additional stabilization of the final inhibitor-protein complex results from hydrogen bonding with His41 which is different for His41ε and His41δ caused by the different geometry. In His41ε there is a OH<sub>b</sub> interaction ( $R = 2.049 \text{ \AA}$  and BSO  $n = 0.226$ ) whereas His41δ benefits from a somewhat stronger NH<sub>a</sub> interaction ( $R = 1.872 \text{ \AA}$  and BSO  $n = 0.375$ ) contributing to the stability as reflected by the more exothermic character of this reaction. Overall, the analysis favors His41δ over His41ε and suggests that the design of inhibitor modifications should focus on weakening the keto CO bond and increasing the CS interaction in the reactant complex. We are currently analyzing recently suggested inhibitor modifications in this regard aiming at adding more points to Fig. 12, i.e., identifying inhibitors with CS bonds in final complex with BSO  $n$  values closer to 1.0 or even above (see Fig. 12(c)) and starting keto CO double bonds with BSO  $n$  values below 1.8 (see Fig. 12(b)).

#### 4 Computational Details

The reaction of the Au-catalyzed Claisen rearrangement and the Re-catalyzed transformation of CO<sub>2</sub> were performed with the popular hybrid density functional B3LYP<sup>272–275</sup> using Stuttgart-Dresden effective core potentials (SDD)<sup>276</sup> with the corresponding basis sets for the Au and the Re atoms accounting for relativistic effects;<sup>277</sup> for all atoms of the Au complexes Pople's 6–31+G(d,p) basis set<sup>278–280</sup> and for all atoms of the Re-complexes Pople's 6–31G(d,p) basis sets were utilized.<sup>278,279</sup> We used in this study as reaction path the intrinsic reaction coordinate (IRC) path of Fukui which follows the reaction path in mass-weighted Cartesian coordinates.<sup>281</sup> It is important to note that the use of mass-weighted coordinates allows for a one-to-one comparison of reaction and curvature profiles of reaction with different substituents or reactions in different media, i.e., gas phase versus solution or enzyme environment.<sup>31,87,101</sup> All

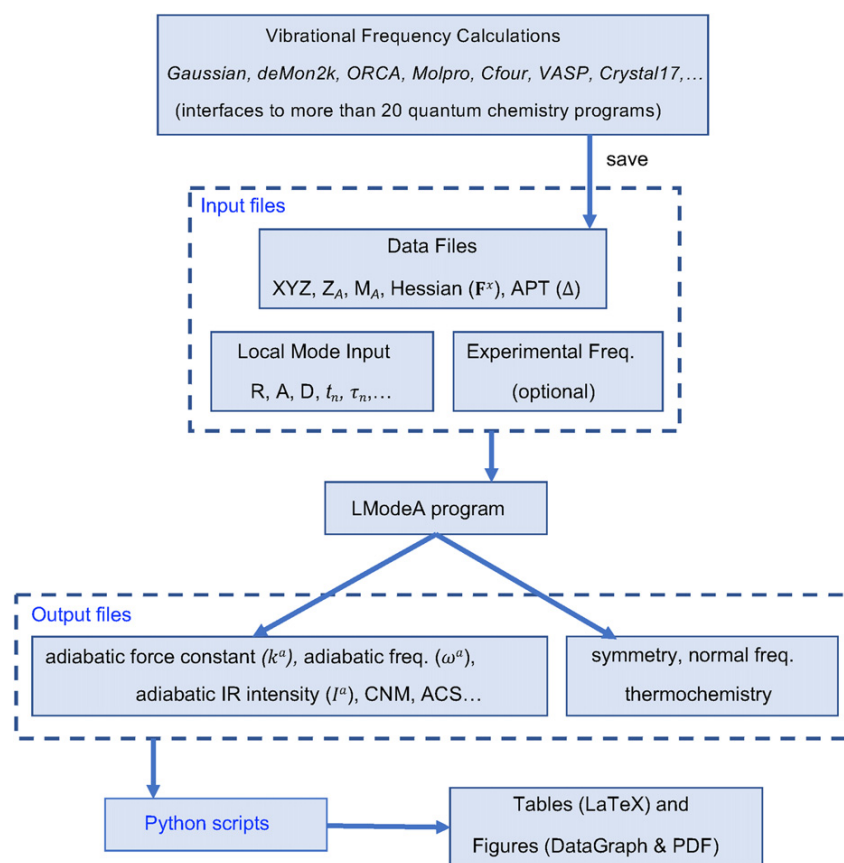


**Fig. 14** Flowchart of the LMODEA software. Reprinted with permission from Kraka E, Zou W, Tao Y. Decoding Chemical Information from Vibrational Spectroscopy Data: Local Vibrational Mode Theory. WIREs: Comput Mol Sci. 2020;10:1480. copyright 2020 from Wiley.

IRC calculations were performed using an ultrafine grid and a tight convergence criterion with a step size of  $s = 0.03 \text{ amu}^{1/2} \text{ Bohr}$ , applying the reaction path following procedure of Hratchian and Kraka, which allows for precise calculations at the enter and exit channels of the reaction.<sup>282</sup> The calculations of the reaction between  $\alpha$ -ketoamide inhibitor and the SARS-CoV-2M<sup>pro</sup> were started from the available crystal structure (PDB: 6Y2G, chain A).<sup>283</sup> The reaction in the gas phase was calculated at the B3LYP/6–31G(d,p) level of theory, and the reaction in the protein was calculated for two protonation forms, His41 (His41 $\epsilon$  and His41 $\delta$ ) located close the reaction site. The inhibitor was placed in the active site of the enzyme using the TS geometry from the gas-phase calculations. The entire protein system was neutralized by 4 Na<sup>+</sup> ions, and surrounded by a TIP3P<sup>284</sup> water sphere of a 16 Å radius centered at the protein active site, in order to mimic a water solution environment. The energy of the protein, the water, and the inhibitor was minimization using AMBER<sup>285</sup> separately for the His45 $\epsilon$  and His45 $\delta$  protonation forms with the frozen inhibitor geometry. Hydrogen atoms were placed according to standard rules of the AMBER force field. The minimized protein structure was divided into a QM part, which included the inhibitor and the side chain of Cys145, while the MM part included the rest of the protein and water atoms. A H linker atom was placed on the side chain of Cys145 in order to fill correct valences of the QM subsystem. The QM/MM TS geometry optimization was followed by the IRC calculations, which were performed with the ONIOM method<sup>286</sup> and applying the B3LYP/6–31G(d,p)/AMBER level of theory, and using an ultrafine grid with the IRC step size of  $s = 0.05 \text{ amu}^{1/2} \text{ Bohr}$ . The URVA calculations were performed with the program pURVA,<sup>287</sup> and the local mode analysis was performed with the LmodeA program.<sup>288</sup> The density functional theory calculations were carried out with Gaussian09.<sup>289</sup>

## 5 Conclusions

We introduce in this article two new tools for the analysis of bond forming/breaking processes taking place during catalytic reactions, the Unified Reaction Valley Approach (URVA) and the Local Mode Analysis (LMA), both being based on vibrational spectroscopy, describing how these new tools complement existing computational strategies, and elucidate URVA and LMA with three examples, two from homogenous catalysis: Au-catalyzed[3,3]-sigmatropic rearrangement of allyl acetate, Re-catalyzed CO<sub>2</sub> cycloaddition to epoxides, and one from enzyme catalysis: $\alpha$ -ketoamide inhibitor for SARS-CoV-2 main protease. In each case the

following protocol is applied: First the non-catalyzed reaction is analyzed, in particular with regard to chemical events which cause a high barrier; then the catalyzed reaction is analyzed and the specifics of the catalyst are decrypted.

URVA records all chemical events as the RC moves along the RP from the entrance channel through the TS into the exit channel leading to the final products. All chemical events can be disclosed by analyzing the curvature of the RP. Different types of chemical reactions are characterized by different curvature profiles (i.e., patterns of curvature minima and maxima), which can serve as their *fingerprints*. A unique decomposition of the path curvature into internal coordinate components provides comprehensive insights into the origins of all chemical changes taking place. Energy demanding chemical events such as bond cleavage taking place before the TS and as such contribute to the activation energy can be identified. This information is in particular valuable in catalysis, helping to modify existing and or to design new catalyst and catalytic cycles.

LMA decodes information on the electronic structure of a compound, the strength of its bonds, its geometry, and its conformational flexibility is contained in the normal vibrational modes. However, these modes are generally delocalized caused by a coupling of the atomic movements during the vibration, which hinders the direct access to this valuable information. LMA provides a unique solution to this problem by extracting local vibrational modes and related local properties from the fundamental normal modes. Local mode stretching force constants quantify the main contributions to bonding and weak chemical interactions in a compound due to specific atom-atom interactions, providing first-hand information for the fine-tuning and designing of new materials as well as shedding light into the frequent suggestion that in catalysis the barrier is lowered because of specifically strong bonding in the TS.

Although catalysis can have many different facets, URVA studies suggest that there are only a few electronic principles that are characteristic of catalysis. Overall we find that in catalytic reactions breaking/forming bonds generally stretch over several reaction phases which demands less energy than bond breaking/forming in just one phase, which is often the case in small organic reactions.<sup>98</sup> More specific results concerning the three examples presented in this article are:

- The Au(I) catalyst in the Au-catalyzed[3,3]-sigmatropic rearrangement of allyl acetate features barrier lowering via a split-up of the non-catalyzed reaction into two reaction steps by acting as a *chameleon*, e.g., easily switching between Au[I]- $\pi$  and Au[I]- $\sigma$  complexation. The catalytic action of the Au[I] catalyst of allyl acetate is due to (1) the formation of a stable  $\sigma$ -bonded intermediate avoiding to start with an energy-consuming breakage of a CO bond; (2) simplification of the ring pseudo-rotation, i.e., no need to bring the RC into a boat form and (3) the assistance of gold with the breaking and forming of the CO bonds.
- The Re-catalyzed CO<sub>2</sub> cycloaddition to epoxides shows another type of catalysis, the coordination-sphere-driven catalysis, often found for transition metal catalysts which facilitate costly bond forming/breaking events by changing the coordination sphere of the transition metal. The key role of the Re-catalyst is to mediate and support the coupling of CO<sub>2</sub> and oxirane via the formation and cleavage of a series of ReC and ReO bonds, which in each of the different steps stretches over several reaction phases, and as such imply a series of small energy-saving changes rather than an abrupt change consuming a larger amount of energy. In addition, the Re atom changes its coordination sphere as needed to facilitating the coupling reaction.
- The  $\alpha$ -ketoamide inhibitor for SARS-CoV-2 main protease study features a combined URVA and LMA QM/MM enzyme study with the objective to explore mechanism of CS bond formation between the inhibitor and Cyst145 of SARS-CoV-2M<sup>pro</sup> and the assessment of the strength of this CS bond in the final complex, which plays a key role for blocking the replication of the corona virus. URVA reveals that for both possible protein forms (His41 $\epsilon$  and His41 $\delta$  protonation form) the reaction barrier is lowered by moving the finalization of the OH bond as well as SH bond cleavage and CO bond adjustment, the essential feature of the reaction, into a post-TS phase, so that these events do not longer contribute to the energy barrier. LMA shows that final inhibitor-protein complex His41 $\delta$  has the strongest CS bond with a BSO  $n$  value of 0.850 compared with BSO  $n$  values of 0.819 for His41 $\epsilon$  and 0.760 for the gas phase reaction. In this regard LMA is the perfect tool for identifying inhibitors leading to CS bonds with BSO  $n$  values close to 1.0 or even above.

In summary, we hope that this article will attract the attention of the computational community to URVA and LMA, so that in the future URVA and LMA will be frequently applied as mechanistic tools to a broad range of chemical reactions, in particular catalytic reactions, and that both URVA and LMA will also enter the classroom.

## 6 Acknowledgments

This work was financially supported by the National Science Foundation (Grant CHE 2102461). We thank SMU for providing generous computational resources. We also thank Alexis Delgado for proof reading.

## Appendix A Supplementary Material

Supplementary data associated with this article can be found in the online version at doi:10.1016/B978-0-12-821978-2.00005-2.

## References

1. Cornils, B., Herrmann, W.A., Xu, J., Zanthoff, H.W. (Eds.), 2020. *Catalysis from A to Z: A Concise Encyclopedia*, fifth ed. New York: Wiley.
2. Paul, C.J.K., Vogt, D., Thybaut, J. (Eds.), 2017. *Contemporary Catalysis: Science, Technology, and Applications*. London: Royal Society of Chemistry.
3. Ruiz, J.C.S. (Ed.), 2017. *Applied Industrial Catalysis*. New York: Arcler Press LLC.
4. Ludwig, J.R., Schindler, C.S., 2017. Catalyst: Sustainable catalysis. *Chem* 2, 313–316.
5. Zhou, Q.L., 2016. Transition-metal catalysis and organocatalysis: Where can progress be expected? *Angew. Chem. Int. Ed.* 55 (18), 5352–5353.
6. Grand View Research I. *Catalyst Market Size*; 2019. San Francisco, CA.
7. van der Hoeven, M., Kobayashi, Y., Diercks, R. (Eds.), 2013. *Technology Roadmap Energy and GHG Reductions in the Chemical Industry via Catalytic Processes*. IEA Publications.
8. Tripathi, P., Sinha, S., 2020. Industrial biocatalysis: An insight into trends and future directions. *Curr. Sustain. Renew. Energy Rep.* 1–7.
9. Sandoval, B.A., Hyster, T.K., 2020. Emerging strategies for expanding the toolbox of enzymes in biocatalysis. *Curr. Opin. Chem. Bio.* 55, 45–51.
10. Chen, K., Arnold, F.H., 2020. Engineering new catalytic activities in enzymes. *Nat. Catal.* 3, 203–213.
11. Chowdhury, R., Maranas, C.D., 2020. From directed evolution to computational enzyme engineering-A review. *AIChE J.* 66, e16847-1-e16847-17.
12. Bilal, M., Cui, J., Iqbal, H.M.N., 2020. Directed evolution of artificial metalloenzymes: A universal means to tune the selectivity of transition metal catalysts? *Acc. Chem. Res.* 52, 336–344.
13. Reilley, D.J., Hennefarth, M.R., Alexandrova, A.N., 2020. The case for enzymatic competitive metal affinity methods. *ACS Catal.* 7, 296-1-296-22.
14. Bilal, M., Cui, J., Iqbal, H.M.N., 2020. The case for enzymatic competitive metal affinity methods. *Int. J. Biol. Macromol.* 130, 186–196.
15. Adams, J.P., Brown, M.J.B., Díaz-Rodríguez, A., Lloyd, R.C., Roiban, G.D., 2019. Biocatalysis: A Pharma Perspective. *Adv. Synth. Catal.* 361 (11), 2421–2432.
16. The Nobel Prize. Accessed: 2021-11-14. <https://www.nobelprize.org>.
17. Benaglia, M., 2021. *Organocatalysis*. New York: de Gruyter.
18. Hartwig, J., 2019. *Organotransition Metal Chemistry: From Bonding to Catalysis*. Mill Valley, California: University Science books.
19. Lan, Y., 2021. *Computational Methods in Organometallic Catalysis: From Elementary Reactions to Mechanisms*. New York: Wiley.
20. Ahn, S., Hong, M., Sundararajan, M., Ess, D.H., Baik, M.H., 2019. Design and optimization of catalysts based on mechanistic insights derived from quantum chemical reaction modeling. *Chem. Rev.* 119, 6509–6560.
21. Durand, D.J., Fey, N., 2019. Computational ligand descriptors for catalyst design. *Chem. Rev.* 119, 6561–6594.
22. Vogiatzis, K.D., Polynski, M.V., Kirkland, J.K., *et al.*, 2019. Computational approach to molecular catalysis by 3d transition metals: Challenges and opportunities. *Chem. Rev.* 119, 2453–2523.
23. Quesne, M.G., Silveri, F., de Leeuw, N.H., Catlow, C.R.A., 2019. Advances in sustainable catalysis: A computational perspective. *Front. Chem.* 7, 182–205.
24. Harvey, J.N., 2019. Mechanism and kinetics in homogeneous catalysis: A computational viewpoint. In: Borowski, E., Borowski, T., Mariusz, R. (Eds.), *Transition Metals in Coordination Environments. Challenges and Advances in Computational Chemistry and Physics* 29. New York: Springer, pp. 289–314.
25. Grajciar, L., Heard, C.J., Bondarenko, A.A., Polynski, M.V., Nachtigall, P., 2018. Towards operando computational modeling in heterogeneous catalysis. *Chem. Soc. Rev.* 47, 8307–8348.
26. Lam, Y., Grayson, M.N., Holland, M.C., Simon, A., Houk, K.N., 2016. Theory and modeling of asymmetric catalytic reactions. *Acc. Chem. Res.* 49, 750–762.
27. Foscatto, M., Jensen, V.R., 2020. Automated in silico design of homogeneous catalysts. *ACS Catal.* 10, 2354–2377.
28. dos Passos Gomes, G., Pollice, R., Aspuru-Guzik, A., 2021. Navigating through the maze of homogeneous catalyst design with machine learning. *Trends Chem.* 3 (2), 96–110.
29. Toyao, T., Maeno, Z., Takakusagi, S., *et al.*, 2020. Machine learning for catalysis informatics: Recent applications and prospects. *ACS Catal.* 10, 2260–2297.
30. von Burg, V., Low, G.H., Häner, T., *et al.*, 2021. Quantum computing enhanced computational catalysis. *Phys. Rev. Res.* 3, 033055-1-033055-16.
31. Kraka, E., Zou, W., Tao, Y., Freindorf, M., 2020. Exploring the mechanism of catalysis with the unified reaction valley approach (URVA) - A review. *Catalysts* 10, 691.
32. Kraka, E., Zou, W., Tao, Y., 2020. Decoding chemical information from vibrational spectroscopy data: Local vibrational mode theory. *WIREs: Comput. Mol. Sci.* 10, 1480.
33. Freindorf, M., Tao, Y., Sethio, D., Cremer, D., Kraka, E., 2018. New mechanistic insights into the claisen rearrangement of chorismate - a unified reaction valley approach study. *Mol. Phys.* 117, 1172–1192.
34. Espinosa-García, J., Monge-Palacios, M., Corchado, J.C., 2012. Constructing potential energy surfaces for polyatomic systems: Recent progress and new problems. *Adv. Phys. Chem.* 2012, 164752-1-164752-19.
35. Rybkin, V.V., 2020. Sampling potential energy surfaces in the condensed phase with many-body electronic structure methods. *Chem. - A Eur. J.* 26 (2), 362–368.
36. Quintas-Sánchez, E., Dawes, R., 2019. AUTOSURF: A freely available program to construct potential energy surfaces. *J. Chem. Inf. Model.* 59 (1), 262–271.
37. Dewyer, A.L., Argüelles, A.J., Zimmerman, P.M., 2018. Methods for exploring reaction space in molecular systems. *WIREs* 8 (2), e1354.
38. Unke, O.T., Koner, D., Patra, S., Käser, S., Meuwly, M., 2020. High-dimensional potential energy surfaces for molecular simulations: From empiricism to machine learning. *Mach. Learn. Sci. Technol.* 1 (1), 013001.
39. Noé, F., Tkatchenko, A., Müller, K.R., Clementi, C., 2020. Machine learning for molecular simulation. *Annu. Rev. Phys. Chem.* 71 (1), 361–390.
40. Abbott, A.S., Turney, J.M., Zhang, B., *et al.*, 2019. PES-Learn: An open-source software package for the automated generation of machine learning models of molecular potential energy surfaces. *J. Chem. Theory Comput.* 15 (8), 4386–4398.
41. Quapp, W., Hirsch, M., Heidrich, D., 2000. Following the streambed reaction on potential-energy surfaces: A new robust method. *Theor. Chem. Acc.* 105, 145–155.
42. Bofill, J.M., Anglada, J.M., 2001. Finding transition states using reduced potential-energy surfaces. *Theor. Chem. Acc.* 105 (6), 463–472.
43. Schlegel, H.B., 2003. Exploring potential energy surfaces for chemical reactions: An overview of some practical methods. *J. Comput. Chem.* 24 (12), 1514–1527.
44. Hirsch, M., Quapp, W., 2004. The reaction pathway of a potential energy surface as curve with induced tangent. *Chem. Phys. Lett.* 395 (1), 150–156.
45. Aguilar-Mogas, A., Giménez, X., Bofill, J.M., 2008. Finding reaction paths using the potential energy as reaction coordinate. *J. Chem. Phys.* 128 (10), 104102.
46. Kim, Y., Kim, J.W., Kim, Z., Kim, W.Y., 2018. Efficient prediction of reaction paths through molecular graph and reaction network analysis. *Chem. Sci.* 9 (4), 825–835.
47. Maeda, S., Harabuchi, Y., Takagi, M., *et al.*, 2018. Implementation and performance of the artificial force induced reaction method in the GRRM17 program. *J. Comput. Chem.* 233–250.
48. Maeda, S., Harabuchi, Y., Ono, Y., Taketsugu, T., Morokuma, K., 2015. Intrinsic reaction coordinate: Calculation, bifurcation, and automated search. *Int. J. Quantum Chem.* 115 (5), 258–269.
49. Tsutsumi, T., Ono, Y., Arai, Z., Taketsugu, T., 2018. Visualization of the intrinsic reaction coordinate and global reaction route map by classical multidimensional scaling. *J. Chem. Theory Comput.* 14 (8), 4263–4270.
50. Quapp, W., Bofill, J.M., 2020. Some mathematical reasoning on the artificial force induced reaction method. *J. Comput. Chem.* 41, 629–634.
51. Hare, S.R., Bratholm, L.A., Glowacki, D.R., Carpenter, B.K., 2019. Low dimensional representations along intrinsic reaction coordinates and molecular dynamics trajectories using interatomic distance matrices. *Chem. Sci.* 10 (43), 9954–9968.
52. Bader, R.F.W., 1994. *Atoms in Molecules: A Quantum Theory*. Oxford University Press.
53. Bader, R.F.W., 1998. *Atoms in molecules*. *Chem. Rev.* 1, 64.
54. Savin, A., Nesper, R., Wengert, S., Fässler, T.F., 1997. ELF: The electron localization function. *Angew. Chem. Int. Ed.* 36 (17), 1808–1832.

55. Andrés, J., Gracia, L., Gonzalez-Navarrete, P., Safont, V., 2015. Chemical structure and reactivity by means of quantum chemical topology analysis. *Comput. Theor. Chem.* 1053, 17–30.
56. Andrés, J., Gonzalez-Navarrete, P., Safont, V.S., 2014. Unraveling reaction mechanisms by means of quantum chemical topology analysis. *Int. J. Quantum Chem.* 114, 1239–1252.
57. Polo, V., Andres, J., Berski, S., Domingo, L.R., Silvi, B., 2008. Understanding reaction mechanisms in organic chemistry from catastrophe theory applied to the electron localization function topology. *J. Phys. Chem. A* 112, 7128–7136.
58. Toro-Labbé, A., Gutiérrez-Oliva, S., Murray, J.S., Politzer, P., 2007. A new perspective on chemical and physical processes: The reaction force. *Mol. Phys.* 105, 2619–2625.
59. Urcelay, F., Toro-Labbé, A., Gutiérrez-Oliva, S., 2020. Spectral decomposition of the reaction force constant. *J. Phys. Chem. A* 124, 2372–2379.
60. Rincon, L., Torres, F.J., Mora, J.R., Zambrano, C.H., Rodríguez, V., 2020. A valence bond perspective of the reaction force formalism. *Theor. Chem. Acc.* 139, 313–1–13–10.
61. Geerlings, P., Chamorro, E., Chattaraj, P., *et al.*, 2020. Conceptual density functional theory: Status, prospects, issues. *Theor. Chem. Acc.* 139, 36–1–36–18.
62. Stuyver, T., Proft, F.D., Geerlings, P., Shaik, S., 2020. How do local reactivity descriptors shape the potential energy surface associated with chemical reactions? The valence bond delocalization perspective. *J. Am. Chem. Soc.* 142, 10102–10113.
63. Martino, M., Salvadori, A., Lazzari, F., *et al.*, 2020. Chemical promenades: Exploring potential-energy surfaces with immersive virtual reality. *J. Comput. Chem.* 41 (13), 1310–1323.
64. Yang, Z., Houk, K.N., 2018. The dynamics of chemical reactions: Atomistic visualizations of organic reactions, and homage to vant hoff. *Chem. - A Eur. J.* 24 (16), 3916–3924.
65. Black, K., Liu, P., Xu, L., Doubleday, C., Houk, K.N., 2012. Dynamics, transition states, and timing of bond formation in Diels-Alder reactions. *Proceedings of the National Academy of Sciences of the United States of America* 109 (32), 12860.
66. Meuwly, M., 2019. Reactive molecular dynamics: From small molecules to proteins. *WIREs Comput. Mol. Sci.* 9 (1), e1386.
67. Gissinger, J.R., Jensen, B.D., Wise, K.E., 2017. Modeling chemical reactions in classical molecular dynamics simulations. *Polymer* 128, 211–217.
68. Pratihari, S., Ma, X., Homayoon, Z., Barnes, G.L., Hase, W.L., 2017. Direct chemical dynamics simulations. *J. Am. Chem. Soc.* 3570–3590.
69. Paranjothy, M., Sun, R., Zhuang, Y., Hase, W.L., 2013. Direct chemical dynamics simulations: Coupling of classical and quasiclassical trajectories with electronic structure theory. *WIREs Comput. Mol. Sci.* 3 (3), 296–316.
70. Tsutsumi, T., Harabuchi, Y., Ono, Y., Maeda, S., Taketsugu, T., 2018. Analyses of trajectory on-the-fly based on the global reaction route map. *Phys. Chem. Chem. Phys.* 20 (3), 1364–1372.
71. Atalay, Y., Paquet, E., Viktor, H.L., 2018. Computational methods for Ab Initio molecular dynamics. *Adv. Chem.* 2018, pp. 9839641–1–9839641–14.
72. Bowman, J.M., Czako, G., Fu, B., 2011. High-dimensional ab initio potential energy surfaces for reaction dynamics calculations. *Phys. Chem. Chem. Phys.* 13 (18), 8094–8111.
73. Chmiela, S., Sauceda, H.E., Tkatchenko, A., Müller, K.R., 2020. Accurate molecular dynamics enabled by efficient physically constrained machine learning approaches. In: Schütt, K., Chmiela, S., von Lilienfeld, O., Tkatchenko, A., Tsuda, K., Müller, K. (Eds.), *Machine Learning Meets Quantum Physics, Lecture Notes in Physics*, vol. 968. New York: Springer, pp. 129–154.
74. Jia, W., Wang, H., Chen, M., *et al.*, 2020. Pushing the limit of molecular dynamics with ab initio accuracy to 100 million atoms with machine learning. *Computational Physics*. arXiv:2005.00223 [physics.comp-ph]. <https://doi.org/10.48550/arXiv.2005.00223>.
75. Konkoli, Z., Kraka, E., Cremer, D., 1997. Unified reaction valley approach mechanism of the reaction  $\text{CH}_3 + \text{H}_2 \rightarrow \text{CH}_4 + \text{H}$ . *J. Phys. Chem. A* 101, 1742–1757.
76. Kraka, E., 2011. Reaction path hamiltonian and the unified reaction valley approach. *WIREs Comput. Mol. Sci.* 1, 531–556.
77. Kraka, E., Cremer, D., 2019. Dieter cremer's contribution to the field of theoretical chemistry. *Int. J. Quantum Chem.* 119, e25849.
78. Kraka, E., Cremer, D., 2010. Computational analysis of the mechanism of chemical reactions in terms of reaction phases: Hidden intermediates and hidden transition states. *Acc. Chem. Res.* 43, 591–601.
79. Cremer, D., Kraka, E., 2010. From molecular vibrations to bonding, chemical reactions, and reaction mechanism. *Curr. Org. Chem.* 14, 1524–1560.
80. Hofacker, L., 1963. Quantentheorie chemischer reaktionen. *Z Naturforsch A* 18, 60–619.
81. Marcus, R.A., 1966. On analytical mechanics of chemical reactions. Quantum mechanics of linear collisions. *J. Chem. Phys.* 45, 4493. (4449).
82. Marcus, R.A., 1966. On analytical mechanics of chemical reactions. Classical mechanics of linear collisions. *J. Chem. Phys.* 45, 4500–4504.
83. Marcus, R.A., 1968. Analytical mechanics of chemical reactions. 3. Natural collision coordinates. *J. Chem. Phys.* 49, 2610–2616.
84. Hougen, J.T., Bunker, P.R., Johns, J.W.C., 1970. Vibration- rotation problem in triatomic molecules allowing for a large-amplitude bending vibration. *J. Mol. Spectrosc.* 34, 136–172.
85. Miller, W.H., Handy, N.C., Adams, J.E., 1980. Reaction path Hamiltonian for polyatomic molecules. *J. Chem. Phys.* 72, 99–112.
86. Kato, S., Morokuma, K., 1980. Potential energy characteristics and energy partitioning in chemical reactions: Ab initio MO study of four-centered elimination reaction  $\text{CH}_3\text{CH}_2\text{F} + \text{CH}_2 \rightarrow \text{CH}_2 + \text{HF}$ . *J. Chem. Phys.* 73, 3900–3914.
87. Zou, W., Sexton, T., Kraka, E., Freindorf, M., Cremer, D., 2016. A new method for describing the mechanism of a chemical reaction based on the unified reaction valley approach. *J. Chem. Theory Comput.* 12, 650–663.
88. Joo, H., Kraka, E., Quapp, W., Cremer, D., 2007. The mechanism of a barrierless reaction: hidden transition state and hidden intermediates in the reaction of methylene with ethene. *Mol. Phys.* 105, 2697–2717.
89. Kühnel, W., 2005. *Differential Geometry: Curves - Surfaces - Manifolds*. New York: American Mathematics Society AMS.
90. Page, M., McIver Jr, J.W., 1988. On evaluating the Reaction path Hamiltonian. *J. Chem. Phys.* 88, 922–935.
91. Wilson, E.B., Decius, J.C., Cross, P.C., 1955. *Molecular Vibrations*. New York: McGraw-Hill.
92. Cremer, D., Wu, A., Kraka, E., 2001. The mechanism of the reaction  $\text{FH} + \text{H}_2\text{C}=\text{CH}_2 \rightarrow \text{H}_2\text{C}-\text{CFH}_3$ . Investigation of hidden intermediates with the unified reaction valley approach. *Phys. Chem. Chem. Phys.* 3, 674–687.
93. Cremer, D., Pople, J.A., 1975. General definition of ring puckering coordinates. *J. Am. Chem. Soc.* 97, 1354–1358.
94. Konkoli, Z., Cremer, D., 1998. A new way of analyzing vibrational spectra. I. Derivation of adiabatic internal modes. *Int. J. Quantum Chem.* 67, 1–9.
95. Konkoli, Z., Larsson, J.A., Cremer, D., 1998. A new way of analyzing vibrational spectra. II. Comparison of internal mode frequencies. *Int. J. Quantum Chem.* 67, 11–27.
96. Kraka, E., Cremer, D., 2002. Mechanism and dynamics of organic reactions: 1,2-H shift in methylchlorocarbene. *J. Phys. Org. Chem.* 15, 431–447.
97. Kraka, E., Wu, A., Cremer, D., 2003. Mechanism of the diels-alder reaction studied with the united reaction valley approach: Mechanistic differences between symmetry-allowed and symmetry-forbidden reactions. *J. Phys. Chem. A* 107, 9008–9021.
98. Kraka, E., Zou, W., Freindorf, M., Cremer, D., 2012. Energetics and mechanism of the hydrogenation of  $\text{XH}_n$  for group IV to group VII elements X. *J. Chem. Theory Comput.* 8, 4931–4943.
99. Sexton, T., Kraka, E., Cremer, D., 2016. Extraordinary mechanism of the diels-alder reaction: Investigation of stereochemistry, charge transfer, charge polarization, and biradicaloid formation. *J. Phys. Chem. A* 120, 1097–1111.
100. Freindorf, M., Sexton, T., Kraka, E., Cremer, D., 2013. The mechanism of the cycloaddition reaction of 1,3-dipole molecules with acetylene - an investigation with the unified reaction valley approach. *Theor. Chem. Acc.* 133, 1423.
101. Sexton, T.M., Freindorf, M., Kraka, E., Cremer, D., 2016. A reaction valley investigation of the cycloaddition of 1,3-dipoles with the dipolarophiles ethene and acetylene: Solution of a mechanistic puzzle. *J. Phys. Chem. A* 120, 8400–8418.

102. López, C.S., Faza, O.N., Freindorf, M., Kraka, E., Cremer, D., 2015. Solving the pericyclic-pseudo pericyclic puzzle in the ring-closure reactions of 1,2,4,6-heptatetraene derivatives. *J. Org. Chem.* 81, 404–414.
103. Freindorf, M., Cremer, D., Kraka, E., 2017. Gold(I)-assisted catalysis – A comprehensive view on the [3,3]-sigmatropic rearrangement of allyl acetate. *Mol. Phys.* 116, 611–630.
104. Luo, Y.R., 2007. *Comprehensive Handbook of Chemical Bond Energies*. Boca Raton, FL: Taylor and Francis.
105. Moltved, K.A., Kepp, K.P., 2018. Chemical bond energies of 3d transition metals studied by density functional theory. *J. Chem. Theory Comput.* 14 (7), 3479–3492.
106. Morse, M.D., 2018. Predissociation measurements of bond dissociation energies. *Acc. Chem. Res.* 52 (1), 119–126.
107. Stasyuk, O.A., Sedlak, R., Guerra, C.F., Hobza, P., 2018. Comparison of the DFT-SAPT and canonical EDA Schemes for the energy decomposition of various types of noncovalent interactions. *J. Chem. Theory Comput.* 14 (7), 3440–3450.
108. Levine, D.S., Head-Gordon, M., 2017. Energy decomposition analysis of single bonds within Kohn-Sham density functional theory. *Proc. Natl. Acad. Sci. USA* 114 (48), 12649–12656.
109. Zhao, L., Hermann, M., Schwarz, W.H.E., Frenking, G., 2019. The Lewis electron-pair bonding model: Modern energy decomposition analysis. *Nat. Rev. Chem.* 3, 49–62.
110. Zhao, L., Pan, S., Holzmann, N., Schwerdtfeger, P., Frenking, G., 2019. Chemical bonding and bonding models of main-group compounds. *Chem. Rev.* 119, 8781–8845.
111. Gavezotti, A., 2016. Comparing the strength of covalent bonds, intermolecular hydrogen bonds and other intermolecular interactions for organic molecules: X-ray diffraction data and quantum chemical calculations. *New J. Chem.* 40, 6848–6853.
112. Robinson, P.J., Alexandrova, A.N., 2015. Assessing the bonding properties of individual molecular orbitals. *J. Phys. Chem. A* 119, 12862–12867.
113. Andrés, J., Ayers, P.W., Boto, R.A., *et al.*, 2019. Nine questions on energy decomposition analysis. *J. Comput. Chem.* 40, 2248–2283.
114. Stewart, J.J.P., 2018. An examination of the nature of localized molecular orbitals and their value in understanding various phenomena that occur in organic chemistry. *J. Mol. Model.* 25, 7.1–17.
115. Kalescky, R., Kraka, E., Cremer, D., 2014. Are carbon-halogen double and triple bonds possible? *Int. J. Quantum Chem.* 114, 1060–1072.
116. Kalescky, R., Zou, W., Kraka, E., Cremer, D., 2014. Quantitative assessment of the multiplicity of carbon-halogen bonds: carbenium and halonium ions with F, Cl, Br, and I. *J. Phys. Chem. A* 118, 1948–1963.
117. Oliveira, V., Kraka, E., Cremer, D., 2016. Quantitative assessment of halogen bonding utilizing vibrational spectroscopy. *Inorg. Chem.* 56, 488–502.
118. Setiawan, D., Sethio, D., Cremer, D., Kraka, E., 2018. From strong to weak NF bonds: On the design of a new class of fluorinating agents. *Phys. Chem. Chem. Phys.* 20, 23913–23927.
119. Sethio, D., Oliveira, V., Kraka, E., 2018. Quantitative assessment of tetrel bonding utilizing vibrational spectroscopy. *Molecules* 23, 2763–1–2763-21.
120. Kraka, E., Cremer, D., 2009. Characterization of CF bonds with multiple-bond character: Bond lengths, stretching force constants, and bond dissociation energies. *ChemPhysChem* 10, 686–698.
121. Cremer, D., Larsson, J.A., Kraka, E., 1998. New developments in the analysis of vibrational spectra on the use of adiabatic internal vibrational modes. In: Parkanyi, C. (Ed.), *Theoretical and Computational Chemistry*. Amsterdam: Elsevier, pp. 259–327.
122. Konkoli, Z., Cremer, D., 1998. A new way of analyzing vibrational spectra. III. Characterization of normal vibrational modes in terms of internal vibrational modes. *Int. J. Quantum Chem.* 67, 29–40.
123. Kaupp, M., Danovich, D., Shaik, S., 2017. Chemistry is about energy and its changes: A critique of bond-length/bond-strength correlations. *Coord. Chem. Rev.* 344, 355–362.
124. Murray, J.S., Politzer, P., 2017. Molecular electrostatic potentials and noncovalent interactions. *WIREs Comput. Mol. Sci.* 7, e1326.
125. Bader, R.F.W., 1991. A quantum theory of molecular structure and its applications. *Chem. Rev.* 91 (5), 893–928.
126. Bader, R.F.W., 1994. *Atoms in Molecules: A Quantum Theory (International Series of Monographs on Chemistry)*. Clarendon Press.
127. Popelier, P.L., 2000. *Atoms in Molecules: An Introduction*. Prentice Hall.
128. Bader, R.F.W., 1998. A bond path: A universal indicator of bonded interactions. *J. Phys. Chem. A* 102 (37), 7314–7323.
129. Jablonski, M., 2019. On the uselessness of bond paths linking distant atoms and on the violation of the concept of privileged exchange channels. *ChemistryOpen* 8, 497–507.
130. Jablonski, M., 2018. Bond paths between distant atoms do not necessarily indicate dominant interactions. *J. Comput. Chem.* 39 (26), 2183–2195.
131. Wick, C.R., Clark, T., 2018. On bond-critical points in QTAIM and weak interactions. *J. Mol. Model.* 24, 142.1–9.
132. Shahbazian, S., 2018. Why bond critical points are not "bond" critical points. *Chem. Eur. J.* 24, 5401–5405.
133. Bader, R.F.W., 2009. Bond paths are not chemical bonds. *J. Phys. Chem. A* 113, 1039–10396.
134. Stöhr, M., Voorhis, T.V., Tkatchenko, A., 2019. Theory and practice of modeling van der Waals interactions in electronic-structure calculations. *Chem. Soc. Rev.* 48, 4118–4154.
135. Kalescky, R., Kraka, E., Cremer, D., 2013. Description of aromaticity with the help of vibrational spectroscopy: Anthracene and phenanthrene. *J. Phys. Chem. A* 118, 223–237.
136. Badger, R.M., 1934. A relation between internuclear distances and bond force constants. *J. Chem. Phys.* 2, 128–131.
137. Kraka, E., Larsson, J.A., Cremer, D., 2010. Generalization of the badger rule based on the use of adiabatic vibrational modes. In: Grunenberg, J. (Ed.), *Computational Spectroscopy*. New York: Wiley, pp. 105–149.
138. Herzberg, G., 1945. *Molecular Spectra and Molecular Structure, II. Infrared and Raman Spectra of Polyatomic Molecules*. New York: Van Nostrand.
139. Konkoli, Z., Larsson, J.A., Cremer, D., 1998. A new way of analyzing vibrational spectra. IV. Application and testing of adiabatic modes within the concept of the characterization of normal modes. *Int. J. Quantum Chem.* 67, 41–55.
140. Wilson, E.B., Decius, J.C., Cross, P.C., 1955. *Molecular vibrations. The Theory of Infrared and Raman Vibrational Spectra*. New York: McGraw-Hill.
141. Woodward, L.A., 1972. *Introduction to the Theory of Molecular Vibrations and Vibrational Spectroscopy*. Oxford: Oxford University Press.
142. Califano, S., 1976. *Vibrational States*. New York: Wiley.
143. Wilson Jr, E.B., 1939. A method of obtaining the expanded secular equation for the vibration frequencies of a molecule. *J. Chem. Phys.* 7, 1047.
144. Neto, N., 1984. Tensor formalism in anharmonic calculations. *Chem. Phys.* 91, 89.
145. Stare, J., 2007. First-principle calculation of reduced masses in vibrational analysis using generalized internal coordinates: Some crucial aspects and examples. *J. Chem. Inf. Model.* 47 (3), 840–850.
146. Zou, W., Kalescky, R., Kraka, E., Cremer, D., 2012. Relating normal vibrational modes to local vibrational modes with the help of an adiabatic connection scheme. *J. Chem. Phys.* 137, 084114.
147. Zou, W., Cremer, D., 2014. Properties of local vibrational modes: The infrared intensity. *Theor. Chem. Acc.* 133, 1451–1466.
148. Zou, W., Cremer, D., 2016. C<sub>2</sub> in a box: Determining its intrinsic bond strength for the X<sup>1</sup> Σ<sub>g</sub><sup>+</sup> ground state. *Chem. Eur. J.* 22, 4087–4097.
149. Delgado, A.A.A., Humason, A., Kalescky, R., Freindorf, M., Kraka, E., 2021. Exceptionally long covalent cc bonds – a local vibrational mode study. *Molecules* 26, 950-1–950-25.
150. Kalescky, R., Kraka, E., Cremer, D., 2013. Identification of the strongest bonds in chemistry. *J. Phys. Chem. A* 117, 8981–8995.
151. Kraka, E., Setiawan, D., Cremer, D., 2015. Re-evaluation of the bond length-bond strength rule: The stronger bond is not always the shorter bond. *J. Comput. Chem.* 37, 130–142.
152. Sethio, D., Lawson Daku, L.M., Hagemann, H., Kraka, E., 2019. Quantitative assessment of B-B-B, B-H<sub>b</sub>-B, and B-H<sub>t</sub> Bonds: From BH<sub>3</sub> to B<sub>12</sub>H<sub>12</sub><sup>2-</sup>. *ChemPhysChem* 20, 1967–1977.

153. Freindorf, M., Yannacone, S., Oliveira, V., Verma, N., Kraka, E., 2021. Halogen bonding involving  $I^2$  and  $d^8$  transition-metal pincer complexes. *Crystals* 11, 373–1–373–21.
154. Oliveira, V., Kraka, E., Cremer, D., 2016. The intrinsic strength of the halogen bond: Electrostatic and covalent contributions described by coupled cluster theory. *Phys. Chem. Chem. Phys.* 18, 33031–33046.
155. Oliveira, V., Cremer, D., 2017. Transition from metal–ligand bonding to halogen bonding involving a metal as halogen acceptor: A study of Cu, Ag, Au, Pt, and Hg complexes. *Chem. Phys. Lett.* 681, 56–63.
156. Yannacone, S., Oliveira, V., Verma, N., Kraka, E., 2019. A continuum from halogen bonds to covalent bonds: Where Do  $\lambda^3$  iodanes Fit? *Inorganics* 7, 47.
157. Oliveira, V.P., Marcial, B.L., Machado, F.B.C., Kraka, E., 2020. Metal–halogen bonding seen through the eyes of vibrational spectroscopy. *Materials* 13, 55.
158. Oliveira, V., Cremer, D., Kraka, E., 2017. The many facets of chalcogen bonding: described by vibrational spectroscopy. *J. Phys. Chem. A* 121, 6845–6862.
159. Oliveira, V., Kraka, E., 2017. Systematic coupled cluster study of noncovalent interactions involving halogens, chalcogens, and pnictogens. *J. Phys. Chem. A* 121, 9544–9556.
160. Setiawan, D., Kraka, E., Cremer, D., 2015. Hidden bond anomalies: The peculiar case of the fluorinated amine chalcogenides. *J. Phys. Chem. A* 119, 9541–9556.
161. Setiawan, D., Kraka, E., Cremer, D., 2014. Strength of the pnictogen bond in complexes involving group VA elements N, P, and As. *J. Phys. Chem. A* 119, 1642–1656.
162. Setiawan, D., Kraka, E., Cremer, D., 2014. Description of pnictogen bonding with the help of vibrational spectroscopy—the missing link between theory and experiment. *Chem. Phys. Lett.* 614, 136–142.
163. Setiawan, D., Cremer, D., 2016. Super-pnictogen bonding in the radical anion of the fluorophosphine dimer. *Chem. Phys. Lett.* 662, 182–187.
164. Freindorf, M., Kraka, E., Cremer, D., 2012. A comprehensive analysis of hydrogen bond interactions based on local vibrational modes. *Int. J. Quantum Chem.* 112, 3174–3187.
165. Kalescky, R., Zou, W., Kraka, E., Cremer, D., 2012. Local vibrational modes of the water dimer – comparison of theory and experiment. *Chem. Phys. Lett.* 554, 243–247.
166. Kalescky, R., Kraka, E., Cremer, D., 2013. Local vibrational modes of the formic acid dimer – The strength of the double H-bond. *Mol. Phys.* 111, 1497–1510.
167. Tao, Y., Zou, W., Jia, J., Li, W., Cremer, D., 2017. Different ways of hydrogen bonding in water – why does warm water freeze faster than cold water? *J. Chem. Theory Comput.* 13, 55–76.
168. Tao, Y., Zou, W., Kraka, E., 2017. Strengthening of hydrogen bonding with the push-pull effect. *Chem. Phys. Lett.* 685, 251–258.
169. Makos, M.Z., Freindorf, M., Sethio, D., Kraka, E., 2019. New insights into Fe–H<sup>+</sup> and Fe–H<sup>-</sup> bonding of a [NiFe] hydrogenase mimic – a local vibrational mode study. *Theor. Chem. Acc.* 138, 76.
170. Lyu, S., Beiranvand, N., Freindorf, M., Kraka, E., 2019. Interplay of ring puckering and hydrogen bonding in deoxyribonucleosides. *J. Phys. Chem. A* 123, 7087–7103.
171. Verma, N., Tao, Y., Kraka, E., 2021. Systematic detection and characterization of hydrogen bonding in proteins via local vibrational modes. *J. Phys. Chem. B* 125, 2551–2565.
172. Beiranvand, N., Freindorf, M., Kraka, E., 2021. Hydrogen bonding in natural and unnatural base pairs – explored with vibrational spectroscopy. *Molecules* 26, 2268–1–2268–22.
173. Yannacone, S., Freindorf, M., Tao, Y., Zou, W., Kraka, E., 2020. Local vibrational mode analysis of  $\pi$ -hole interactions between aryl donors and small molecule acceptors. *Crystals* 10, 556–1–556–25.
174. Mayer, I., 1983. Charge, bond order and valence in the ab initio theory. *Chem. Phys. Lett.* 97, 270–274.
175. Mayer, I., 1986. Bond orders and valences from ab initio wave functions. *Int. J. Quantum Chem.* 29, 477–483.
176. Mayer, I., 2007. Bond order and valence indices: A personal account. *J. Comput. Chem.* 28 (1), 204–221.
177. Kraka, E., Freindorf, M., 2020. Characterizing the metal ligand bond strength via vibrational spectroscopy: The metal ligand electronic parameter (MLEP). In: Liedós, A., Ujaque, G. (Eds.), *Topics in Organometallic Chemistry – New Directions in the Modeling of Organometallic Reactions* 67. Berlin, Heidelberg: Springer, pp. 1–43.
178. Hashmi, S.K., 2021. Introduction: Gold chemistry. *Chem. Rev.* 121, 8309–8310.
179. Witzel, S., Hashmi, A.S.K., Xie, J., 2021. Light in gold catalysis. *Chem. Rev.* 121, 8868–8925.
180. Pflästerer, D., Hashmi, A.S.K., 2016. Gold catalysis in total synthesis – recent achievements. *Chem. Rev.* 45, 1331–1367.
181. Huang, B., Hu, M., Toste, F.D., 2020. Homogeneous gold redox chemistry: Organometallics, catalysis, and beyond. *Trends Chem.* 2, 707–720.
182. Marín-Luna, M., Faza, O.N., López, C.S., 2019. Gold-catalyzed homogeneous (Cyclo)isomerization reactions. *Front. Chem.* 45, 296–1–296–22.
183. Pyykkö, P., 2008. Theoretical chemistry of gold. III. *Chem. Soc. Rev.* 37, 1967–1997.
184. Pyykkö, P., 2004. Theoretical chemistry of gold. *Angew. Chem. Int. Ed.* 43, 4412–4456.
185. Schwerdtfeger, P., 2002. Relativistic effects in properties of gold. *Heteroat. Chem.* 13, 578–584.
186. Kraka, E., Filatov, M., Cremer, D., 2009. Comparison of gold bonding with mercury bonding. *Croat. Chim. Acta* 82, 233–243.
187. Li, Y., Oliveira, V., Tang, C., Cremer, D., Liu, C., 2017. g Ma J. The peculiar role of the Au<sub>3</sub> Unit in Au<sub>m</sub> clusters:  $\sigma$ -aromaticity of the Au<sub>3</sub>Zn<sup>+</sup> Ion. *Inorg. Chem.* 56, 5793–5803.
188. Li, Y., Liu, C., Oliveira, V., *et al.*, 2018. Odd-even effect of the number of free valence electrons on the electronic structure properties of gold–thiolate clusters. *Mol. Phys.* 117, 1442–1450.
189. Glantschnig, K., Ambrosch-Draxl, C., 2010. Relativistic effects on the linear optical properties of Au, Pt, Pb and W. *New J. Phys.* 12, 103048–1–103048–16.
190. Reis, M.C., López, C.S., Kraka, E., Cremer, D., Faza, O.N., 2016. Rational design in catalysis: A mechanistic study of  $\beta$ -hydride eliminations in Gold(I) and Gold(III) complexes based on features of the reaction valley. *Inorg. Chem.* 55, 8636–8645.
191. Zi, W., Dean, Toste, F., 2016. Recent advances in enantioselective gold catalysis. *Chem. Soc. Rev.* 45, 4567–4589.
192. Kennedy, C.R., Lin, S., Jacobsen, E.N., 2016. The cation– $\pi$  interaction in small-molecule catalysis. *Angew. Chemie Int. Ed.* 55, 12596–12624.
193. Vidhani, D.V., Cran, J.W., Krafft, M.E., Manoharan, M., Alabugin, I.V., 2013. Gold(I)-catalyzed claisen rearrangement of allenyl vinyl ethers: Missing transition states revealed through evolution of aromaticity, Au(I) as an oxophilic lewis acid, and lower energy barriers from a high energy complex. *J. Org. Chem.* 78 (5), 2059–2073.
194. Sherry, B.D., Toste, F.D., 2004. Gold (I)-catalyzed propargyl claisen rearrangement. *J. Am. Chem. Soc.* 14, 15978–15979.
195. Rocchigiani, L., Bochmann, M., 2021. Recent advances in gold(III) chemistry: Structure, bonding, reactivity, and role in homogeneous catalysis. *Chem. Rev.* 121, 8364–8451.
196. Wu, C.Y., Horibe, T., Jacobsen, C.B., Toste, F.D., 2015. Stable gold(III) catalysts by oxidative addition of a carbon–carbon bond. *Nature* 517, 449–454.
197. Comas-Vives, A., González-Arellano, C., Corma, A., *et al.*, 2006. Single-site homogeneous and heteroatomized gold(III) hydrogenation catalysts: Mechanistic implications. *J. Am. Chem. Soc.* 128, 4756–4765.
198. Motloch, P., Jasik, J., Roithová, J., 2021. Gold(I) and silver(I)  $\pi$ -complexes with unsaturated hydrocarbons. *Organometallics* 40, 1492–1502.
199. Collado, A., Nelson, D.J., Nolan, S.P., 2021. Optimizing catalyst and reaction conditions in gold(I) catalysis –ligand development. *Chem. Rev.* 121, 8559–8612.
200. Lu, Z., Li, T., Mudshinge, S.R., Xu, B., Hammond, G.B., 2021. Optimization of catalysts and conditions in Gold(I) catalysis – counterion and additive effects. *Chem. Rev.* 121, 8452–8477.
201. Arduengo, A.J., Harlow, R.L., Kline, M., 1991. A stable crystalline carbene. *J. Am. Chem. Soc.* 113 (1), 361–363.
202. Díez-González, S. (Ed.), 2017. *N-Heterocyclic Carbenes – From Laboratory Curiosities to Efficient Synthetic Tools*. London: Royal Society of Chemistry.
203. Gómez-Suárez, A., Nelson, D.J., Nolan, S.P., 2017. Quantifying and understanding the steric properties of N-heterocyclic carbenes. *Chem. Commun.* 53, 2650–2660.
204. Jacobsen, H., Correa, A., Poater, A., Costabile, C., Cavallo, L., 2009. Understanding the M(NHC) (NHC = N-heterocyclic carbene) bond. *Coord. Chem. Rev.* 253 (5–6), 687–703.
205. Mora, M., Gimeno, M.C., Visbal, R., 2019. Recent advances in gold-NHC complexes with biological properties. *Chem. Soc. Rev.* 48, 447–462.

206. Tang, X.T., Yang, F., Zhang, T.T., *et al.*, 2019. Recent progress in N-Heterocyclic carbene gold-catalyzed reactions of alkynes involving oxidation/amination/cycloaddition. *Catalysis* 10, 350–1–350–23.
207. Makoš, M.Z., Freindorf, M., Tao, Y., Kraka, E., 2021. Theoretical insights into [NHC]Au(I) catalyzed hydroalkoxylation of allenes: A unified reaction valley approach study. *J. Org. Chem.* 86, 5714–5726.
208. Gourlaouen, C., Marion, N., Nolan, S.P., 2009. Mechanism of the (NHC)-Au(I)-catalyzed rearrangement of allylic acetates. A DFT study. *Org. Lett.* 11 (4), 12–15.
209. Lackner, M., Sajjadi, B., Chen, W.Y. (Eds.), 2022. *Handbook of Climate Change Mitigation and Adaptation*, third ed. New York: Springer.
210. Andersen, I., 2021. Emissions Gap Report 2021: The Heat Is On. United Nations Environment Programme.
211. Suárez, J.A., Remesal, E.R., Plata, J.J., Márquez, A.M., Sanz, J.F., 2021. Computational modeling of carbon dioxide catalytic conversion. In: Reina, T.R., Odriozola, J.A., Arellano-García, H. (Eds.), *Engineering Solutions for CO<sub>2</sub> Conversion*, first ed. New York: Wiley-VCH, pp. 85–103.
212. Kumar, A., Sharma, S. (Eds.), 2021. *Chemo-Biological Systems for CO<sub>2</sub> Utilization*. Boca Raton: CRC press, Taylor & Francis Group.
213. Claver, C., Yeamin, M.B., Reguero, M., Masdeu-Bultó, A.M., 2020. New trends in the conversion of CO<sub>2</sub> to cyclic carbonates. *Catalysis* 10, 479–1–479–14.
214. Claver, C., Yeamin, M.B., Reguero, M., Masdeu-Bultó, A.M., 2020. Recent advances in the use of catalysts based on natural products for the conversion of CO<sub>2</sub> into cyclic carbonates. *Green Chem.* 22, 7665–7706.
215. Kiatkittipong, K., Shukri, M.A.A.M., Kiatkittipong, W., *et al.*, 2020. Green pathway in utilizing CO<sub>2</sub> via cycloaddition reaction with epoxide- mini review. *Processes* 8, 548–1–548–22.
216. Songa, X., Wang, J., Yang, L., Pan, H., Zheng, B., 2020. The transformation strategies between homogeneous and heterogeneous catalysts for the coupling reactions of CO<sub>2</sub> and epoxides/olefins. *Inorg. Chem. Commun.* 121, 108197–1–108197–14.
217. Rehman, A., Saleem, F., Javed, F., *et al.*, 2021. Recent advances in the synthesis of cyclic carbonates via CO<sub>2</sub> cycloaddition to epoxides. *J. Environ. Chem. Eng.* 9, 105113–1–105113–28.
218. Nasirov, F., Nasirli, E., Ibrahimova, M., 2021. Cyclic carbonates synthesis by cycloaddition reaction of CO<sub>2</sub> with epoxides in the presence of zinc-containing and ionic liquid catalysts - Review. *J. Iran. Chem. Soc.* 19, 353–379.
219. Pescarmona, P.P., 2021. Cyclic carbonates synthesized from CO<sub>2</sub>: Applications, challenges and recent research trends. *Curr. Opin. Green Sustain. Chem.* 29, 100457–1–100457–9.
220. Jiang, J.L., Gao, F., Hua, R., Qiu, X., 2005. Re(CO)<sub>5</sub>Br-catalyzed coupling of epoxides with CO<sub>2</sub> affording cyclic carbonates under solvent-free conditions. *J. Org. Chem.* 70, 381–383.
221. Guo, C.H., Song, J.Y., Jia, J.F., Zhang, X.M., Wu, H.S., 2010. A DFT study on the mechanism of the coupling reaction between chloromethyloxirane and carbon dioxide catalyzed by Re(CO)<sub>5</sub>Br. *Organometallics* 29, 2069–2079.
222. Wu, S., Snajdrova, R., Moore, J.C., Baldenius, K., Bornscheuer, U.T., 2021. Biocatalysis: Enzymatic synthesis for industrial applications. *Angew. Chem. Int. Ed.* 60, 88–119.
223. Singh, P., Vandemeulebroucke, A., Li, J., *et al.*, 2021. Evolution of the chemical step in enzyme catalysis. *ACS Catal.* 11, 672–6732.
224. Agarwal, P.K., 2019. A biophysical perspective on enzyme catalysis. *Biochemistry* 58, 438–449.
225. Arcus, V.L., van der Kamp, M.W., Pudney, C.R., Mulholland, A.J., 2020. Enzyme evolution and the temperature dependence of enzyme catalysis. *Curr. Opin. Struct. Biol.* 65, 96–101.
226. Warshel, A., Bora, R.P., 2016. Perspective: Defining and quantifying the role of dynamics in enzyme catalysis. *J. Chem. Phys.* 144, 180901–180918.
227. Alonso-Colchico, L., JaimeRodriguez-Guerra, Lledós, A., Marechal, J.D., 2020. Engineering new catalytic activities in enzymes. *Acc. Chem. Res.* 53, 896–905.
228. Schwizer, F., Okamoto, Y., Heinisch, T., *et al.*, 2017. Artificial metalloenzymes: Reaction scope and optimization strategies. *Chem. Rev.* 118, 142–231.
229. Bunzel, H.A., Anderson, L.R., Mulholland, A.J., 2021. Designing better enzymes: Insights from directed evolution. *Curr. Opin. Struct. Biol.* 67, 212–218.
230. Chen, K., Arnold, F.H., 2020. Engineering new catalytic activities in enzymes. *Nat. Catal.* 3, 203–213.
231. Bell, R.P., 1936. The theory of reactions involving proton transfers. *Proc. R. Soc. Lond. Ser. A* 154, 414–429.
232. Evans, M.G., Polanyi, M., 1936. Further considerations on the thermodynamics of chemical equilibria and reaction rates. *J. Chem. Soc. Faraday Trans.* 32, 1333–1360.
233. de Visser, S.P., Lin, Y.T., Ali, H.S., *et al.*, 2021. Negative catalysis/non-Bell-Evans-Polanyi reactivity by metalloenzymes: Examples from mononuclear heme and non-heme iron oxygenases. *Coord. Chem. Rev.* 439, 213914–1–213914–16.
234. Alanagreh, L., Alzoughool, F., Atoum, M., 2020. The human coronavirus disease COVID-19: Its origin, characteristics, and insights into potential drugs and its mechanisms. *Pathogens* 9, 331–1–331–11.
235. Nadeem, M.S., Zamzami, M.A., Choudhry, H., *et al.*, 2020. Origin, potential therapeutic targets and treatment for coronavirus disease (COVID-19). *Pathogens* 9, 307–1–307–13.
236. Platto, S., Wang, Y., Zhou, J., Carafoli, E., 2021. History of the COVID-19 pandemic: Origin, explosion, worldwide spreading. *Biochem. Biophys. Res. Commun.* 538, 14–23.
237. Morens, D.M., Breman, J.G., Calisher, C.H., *et al.*, 2020. The origin of COVID-19 and why it matters. *Am. J. Trop. Med. Hyg.* 103, 955–959.
238. Live coronavirus update. Available at: <https://www.worldometers.info/coronavirus/>.
239. Simran Preet Kaur, V.G., 2020. COVID-19 vaccine: A comprehensive status report. *Virus Res.* 288, 198114–1–198114–12.
240. Consortium, W.S.T., 2021. Repurposed antiviral drugs for Covid-19 - Interim WHO solidarity trial results. *New Engl. J. Med.* 384, 497–511.
241. Bryant, A., Lawrie, T.A., Dowswell, T., *et al.*, 2020. Ivermectin for prevention and treatment of COVID-19 infection: A systematic review, meta-analysis, and trial sequential analysis to inform clinical guidelines. *J. Am. Ther.* 28, e434–e460.
242. Singh, A.K., Singh, A., Singh, R., Misra, A., 2020. Ivermectin for prevention and treatment of COVID-19 infection: A systematic review, meta-analysis, and trial sequential analysis to inform clinical guidelines. *Diabetes Metab. Syndr. Clin. Res. Rev.* 15, 102329–1–102329–12.
243. Guy, R.K., DiPaola, R.S., Romanelli, F., Dutch, R.E., 2020. Rapid repurposing of drugs for COVID-19. *Science* 368, 829–830.
244. Mengist, H.M., Dilnessa, T., Jin, T., 2021. Structural basis of potential inhibitors targeting SARS-CoV-2 main protease. *Front. Mol. Biosci.* 9, 622898–1–622898–19.
245. Cui, W., Yang, K., Yang, H., 2020. Recent progress in the drug development targeting SARS-CoV-2 main protease as treatment for COVID-19. *Front. Mol. Biosci.* 7, 616341–1–616341–10.
246. Swiderek, K., Moliner, V., 2020. Revealing the molecular mechanisms of proteolysis of SARS-CoV-2 Mpro by QM/MM computational methods. *Chem. Sci.* 11 (39), 10626–10630.
247. Robello, M., Barresi, E., Baglini, E., *et al.*, 2021. The alpha keto amide moiety as a privileged motif in medicinal chemistry: Current insights and emerging opportunities. *J. Med. Chem.* 64, 3508–3545.
248. El Hassab, M.A., Fares, M., Abdel-Hamid Amin, M.K., *et al.*, 2021. Toward the identification of potential  $\alpha$ -ketoamide covalent inhibitors for SARS-CoV-2 main protease: Fragment-based drug design and MM-PBSA calculations. *Processes* 9, 1004–1–1004–7714.
249. Zhang, L., Lin, D., Kusov, Y., *et al.*, 2021.  $\alpha$ -Ketoamides as broad-spectrum inhibitors of coronavirus and enterovirus replication: Structure-based design, synthesis, and activity assessment. *J. Med. Chem.* 63, 4562–4578.
250. Mondal, D., Warshel, A., 2020. Exploring the mechanism of covalent inhibition: Simulating the binding free energy of  $\alpha$ -ketoamide inhibitors of the main protease of SARS-CoV-2. *Biochemistry* 59, 4601–4608.
251. Zhang, L., Lin, D., Sun, X., *et al.*, 2020. Crystal structure of SARS-CoV-2 main protease provides a basis for design of improved  $\alpha$ -ketoamide inhibitors. *Science* 368, 409–412.
252. Halford, B., 2020. Covalent drugs go from fringe field to fashionable endeavor. *C&E News* 98, 1–12.

253. Sutanto, F., Konstantinidou, M., Dömling, A., 2020. Covalent inhibitors: A rational approach to drug discovery. *RSC Med. Chem.* 11, 876–884.
254. Aljoundi, A., Bji, I., Rashedy, A.E., Soliman, M.E.S., 2020. Covalent versus non-covalent enzyme inhibition: Which route should we take? A justification of the good and bad from molecular modelling perspective. *Protein J.* 39, 97–105.
255. Hollingsworth, S.A., Dror, R.O., 2018. Molecular dynamics simulation for all. *Neuron* 99, 1129–1143.
256. Zimmer, M., 2009. Are classical molecular mechanics calculations still useful in bioinorganic simulations. *Coord. Chem. Rev.* 253, 817–826.
257. Fröhling, T., Bernetti, M., Calonaci, N., Bussia, G., 2020. Toward empirical force fields that match experimental observables. *J. Chem. Phys.* 152, 230902-1-230902-9.
258. Unke, O.T., Chmiela, S., Sauceda, H.E., *et al.*, 2021. Machine learning force fields. *Chem. Rev.* 121, 10142–10186.
259. hong Lam, Y., Abramov, Y., Ananthula, R.S., *et al.*, 2020. Applications of quantum chemistry in pharmaceutical process development: Current state and opportunities. *Org. Process Res. Dev.* 24, 1496–1507.
260. Senn, H.M., Thiel, W., 2009. QM/MM methods for biomolecular systems. *Angew. Chem. Int. Ed.* 48, 1198–1229.
261. Magalhaes, R.P., Fernandes, H.S., Sousa, S.F., 2020. Modeling enzymatic mechanisms with QM/MM approaches: Current status and future challenges. *Isr. J. Chem.* 60 (1), 13.
262. Himo, F., 2017. Recent trends in quantum chemical modeling of enzymatic reactions. *J. Am. Chem. Soc.* 139, 6780–6786.
263. Quesne, M.G., Borowski, T., de Visser, S.P., 2016. Quantum mechanics/molecular mechanics modeling of enzymatic processes: Caveats and breakthroughs. *Chem. Eur. J.* 22, 2562–2581.
264. Cui, Q., 2016. Perspective: Quantum mechanical methods in biochemistry and biophysics. *J. Chem. Phys.* 145, 140901–140913.
265. Ramirez, C.L., Martí, M.A., Roitberg, A.E., 2016. Chapter 6: Steered Molecular Dynamics Methods Applied to Enzyme Mechanism and Energetics, vol. 578. Amsterdam: Elsevier Inc.
266. Sokkar, P., Boulanger, E., Thiel, W., Sanchez-Garcia, E., 2015. Hybrid quantum mechanics/molecular mechanics/coarse grained modeling: A triple-resolution approach for biomolecular systems. *J. Chem. Theory Comput.* 11, 1809–1818.
267. Lever, G., 2015. A density-functional perspective on the chorismate mutase enzyme. *Large-Scale Quantum-Mechanical Enzymology*. Switzerland: Springer International Publishing, pp. 111–141.
268. Patel, I.S., 2015. Large Scale Simulation And Analysis To Understand Enzymatic Chemical Mechanisms. Cambridge, MA: Massachusetts Institute of Technology, (Department of Chemistry, PhD thesis).
269. Lynch, J.H., Dudareva, N., 2020. Aromatic amino acids: A complex network ripe for future exploration. *Trends Plant Sci.* 1935, 1–12.
270. Mir, R., Jallu, S., Singh, T.P., 2015. The shikimate pathway: Review of amino acid sequence, function and three-dimensional structures of the enzymes. *Crit. Rev. Microbiol.* 41, 172–189.
271. Maeda, H., Dudareva, N., 2015. The shikimate pathway and aromatic amino acid biosynthesis in plants. *Annu. Rev. Plant Biol.* 63, 73–105.
272. Becke, A.D., 1993. Density-functional thermochemistry. III. The role of exact exchange. *J. Chem. Phys.* 98, 5648–5652.
273. Lee, C., Yang, W., Parr, R.G., 1988. Development of the Colle-Salvetti correlation-energy formula into a functional of the electron density. *Phys. Rev. B* 37, 785–789.
274. Vosko, S.H., Wilk, L., Nusair, M., 1980. Accurate spin-dependent electron liquid correlation energies for local spin density calculations: a critical analysis. *Can. J. Phys.* 58, 1200–1211.
275. Stephens, P.J., Devlin, F.J., Chabalowski, C.F., Frisch, M.J., 1994. Ab Initio calculation of vibrational absorption and circular dichroism spectra using density functional force fields. *J. Phys. Chem.* 98, 11623–11627.
276. Schwerdtfeger, P., 2011. The pseudopotential approximation in electronic structure theory. *ChemPhysChem* 12, 3143–3155.
277. Andrae, D., Haeussermann, U., Dolg, M., Stoll, H., Preuss, H., 1990. Energy-adjusted ab initio pseudopotentials for the second and third row transition elements. *Theor. Chim. Acta* 77, 123–141.
278. Ditchfield, D., Hehre, W.J., Pople, J.A., 1971. Self-consistent molecular orbital methods. 9. Extended Gaussian-type basis for molecular-orbital studies of organic molecules. *J. Chem. Phys.* 54, 724–728.
279. Hariharan, P.C., Pople, J.A., 1973. The influence of polarization functions on molecular orbital hydrogenation energies. *Theor. Chim. Acta* 28 (3), 213–222.
280. Frisch, M.J., Pople, J.A., 1984. Self-consistent molecular orbital methods 25. Supplementary functions for Gaussian basis sets. *J. Chem. Phys.* 3265–3269.
281. Fukui, K., 1981. The path of chemical-reactions- the IRC approach. *Acc. Chem. Res.* 14 (363), 368.
282. Hratchian, H.P., Kraka, E., 2013. Improved predictor-corrector integrators for evaluating reaction path curvature. *J. Chem. Theory Comput.* 9, 1481–1488.
283. Linlin, Z., Daizong, L., Xinyuanyuan, S., *et al.*, 2020. Crystal structure of SARS-CoV-2 main protease provides a basis for design of improved  $\alpha$ -ketoamide inhibitors. *Science* 368 (6489), 409–412.
284. Jorgensen, W.L., Chandrasekhar, J., Madura, J.D., Impey, R.W., Klein, M.L., 1983. Comparison of simple potential functions for simulating liquid water. *J. Chem. Phys.* 79, 926–935.
285. Case, D.A., Ben-Shalom, I.Y., Brozell, S.R., *et al.*, 2018. AMBER. San Francisco: University of California.
286. Chung, L.W., Sameera, W.M.C., Ramozzi, R., *et al.*, 2015. The ONIOM Method and Its Applications. *Chem. Rev.* 115, 5678–5796.
287. Tao, Y., Zou, W., Freindorf, M., Cremer, D., Kraka, E., 2021. Computational and Theoretical Chemistry Group ((CATCO)). Dallas, TX: Southern Methodist University, (pURVA).
288. Zou, W., Tao, Y., Freindorf, M., *et al.*, 2021. Local Vibrational Mode Analysis. Dallas, TX, USA: Computational and Theoretical Chemistry Group (CATCO), Southern Methodist University.
289. Frisch, M.J., Trucks, G.W., Schlegel, H.B., *et al.*, 2009. Gaussian, Inc. Gaussian Inc, Wallingford CT.2009